Alma Mater Studiorum
Università degli Studi di Bologna

SCUOLA DI SCIENZE
Dipartimento di Fisica e Astronomia
Corso di Laurea Magistrale in Astrofisica e Cosmologia

Dark matter and stellar populations in the central region of early-type galaxies

Tesi di Laurea Magistrale

Candidato:
Caterina Caravita

Relatore:
Chiar.mo Prof. Luca Ciotti

Corelatore:
Chiar.ma Prof.ssa Silvia Pellegrini

Corelatore:
Dott. Andrea Negri

Sessione III
Anno accademico 2016/2017

Ai miei nonni
Ruggero, Brunella e Mirella.

When I was your age, I always did it for half-an-hour a day.
Why, sometimes I believed as many as six impossible things
before breakfast.
Quando ero giovane, mi esercitavo sempre mezz'ora al giorno.
A volte, riuscivo a credere a sei cose impossibili
prima di colazione.
Lewis Carroll

...allo spazio perché dalle nubi di gas stellari il Sole si condensasse e bruciasse;
alle quantità di stelle e galassie e ammassi galattici in fuga nello spazio
che ci sarebbero volute per tener sospesa ogni galassia ogni nebula
ogni sole ogni pianeta, e nello stesso tempo del pensarlo
questo spazio inarrestabilmente si formava...
Italo Calvino

Abstract

This thesis work is aimed at the investigation of the dark matter (DM) amount and distribution in early-type galaxies (ETGs), in relation with the stellar properties, constrained by observations of the kinematic fields of galaxies. In particular, we focus on observations of the projected stellar velocity dispersion in the central region of ETGs. A robust determination of the DM amount and distribution is an open issue, which we explore from two complementary points of view. A *top-down* approach, with priority given to cosmology, based on the predictions of numerical cosmological simulations, and a *bottom-up* approach, with priority given to the galactic astrophysics. This is accomplished by using the original numerical code JASMINE (Jeans AxiSymmetric Models of galaxies IN Equilibrium), first developed by Posacki et al. (2013), to build dynamical models of ETGs, based on the solution of the Jeans equations. Our Jeans modelling produces axisymmetric (oblate) spheroids with anisotropic stellar orbits. In this thesis work, we focus on spherical isotropic galaxy models, composed of stars, DM and a central supermassive black hole (BH). The stellar component is modelled by a deprojected de Vaucouleurs or Jaffe density profile and satisfies the Faber-Jackson and size-luminosity Scaling Laws. The BH mass, M_{BH}, is related to the total stellar mass, M_*, by the Magorrian relation. The DM component is modelled by the NFW density profile. We explore the effect on the dynamics of stars, due to the stellar and DM properties, such as the assumption of a fixed stellar mass-to-light ratio, $\Upsilon_{*\,dyn}$, and fixed halo parameters β and c (halo-to-stellar scale radius ratio and halo concentration, respectively). We intend to investigate how much the DM amount and distribution can vary, while reproducing a given value for the projected central velocity dispersion of stars, σ_{e8} (luminosity-weighted within $R_e/8$). Our study suggests that σ_{e8} is not a good diagnostic of the DM properties in ETGs, especially it is not able to constrain the DM amount and distribution at large radii. This is a preliminary work which we will extend through the exploration of different properties of ETGs and through observations of their kinematic fields at larger radii (e.g. $R_e/2$, R_e), aiming to better understand their dark and luminous contents.

Sommario

Questo lavoro di tesi è finalizzato all'investigazione della quantità e distribuzione di materia oscura (dall'inglese, DM) nelle galassie *early-type* (ETGs), in relazione alle proprietà stellari, vincolate da osservazioni del campo cinematico delle galassie. In particolare, ci focalizziamo su osservazioni della dispersione di velocità delle stelle nella regione centrale delle ETGs, proiettata lungo la linea di vista. Una robusta determinazione della quantità e distribuzione di DM è un campo di ricerca aperto, che esploriamo da due punti di vista complementari. Un approccio *dall'alto*, che da priorità alla cosmologia, basandosi sulle previsioni delle simulazioni numeriche cosmologiche, e un approccio *dal basso*, cha da priorità all'astrofisica galattica. Questo obiettivo è conseguito utilizzando il codice numerico originale JASMINE (Jeans AxiSymmetric Models of galaxies IN Equilibrium), sviluppato da Posacki et al. (2013), che costruisce modelli dinamici di ETGs, sulla base della risoluzione delle equazioni di Jeans. La nostra modellizzazione di Jeans produce sferoidi assisimmetrici (oblati) con orbite stellari anisotrope. In questo lavoro di tesi, ci siamo concentrati su modelli di galassie sferici e isotropi, costituiti da stelle, materia oscura e un buco nero (BH) centrale supermassiccio. La componente stellare è modellata con un profilo di densità di de Vaucouleurs proiettato o di Jaffe e soddisfa le leggi di scala *Faber-Jackson* e *size-luminosity*. La massa del BH, M_{BH}, è in relazione alla massa stellare totale, M_*, attraverso la relazione di Magorrian. La componente di DM è modellata con un profilo di NFW. Esploriamo gli effetti sulla dinamica delle stelle, dovuti a proprietà stellari e di alone, come l'assunzione di un *mass-to-light ratio* fissato, Υ_{*dyn}, e di fissati parametri di alone β e c (rapporto tra i raggi scala di alone e stellare e parametro di concentrazione dell'alone, rispettivamente). Intendiamo investigare quanto possano variare la quantità e la distribuzione di DM, riproducendo un dato valore della dispersione di velocità centrale proiettata delle stelle, σ_{e8} (pesata sulla luminosità entro $R_e/8$). Il nostro studio suggerisce che σ_{e8} non sia un buon indicatore delle proprietà della DM nelle ETGs, in particolare non è adatta a vincolare la quantità e la distribuzione di DM a grandi raggi. Si tratta di un lavoro preliminare che estenderemo e approfondiremo attraverso l'esplorazione di diverse proprietà delle ETGs e attraverso osservazioni dei loro campi cinematici a raggi maggiori (e.g. $R_e/2$, R_e), con lo scopo di comprendere più a fondo il loro contenuti oscuro e luminoso.

x

Contents

Chapter 1

Introduction

1.1 ETGs and Scaling Laws

The first morphological classification of galaxies is due to E. P. Hubble, who mainly distinguished between elliptical (E) and spiral (S), or disc, galaxies in its empirical *tuning-fork* diagram (Hubble, 1936), shown in figure 1.1. On the left-hand side there are the Es and on the right-hand side the Ss (with or without bar); between them, lenticular galaxies (S0) represent disc without spiral arms; at the end of the diagram, there are the irregular galaxies. Today, it is preferred to distinguish galaxies in the Local Universe (redshift

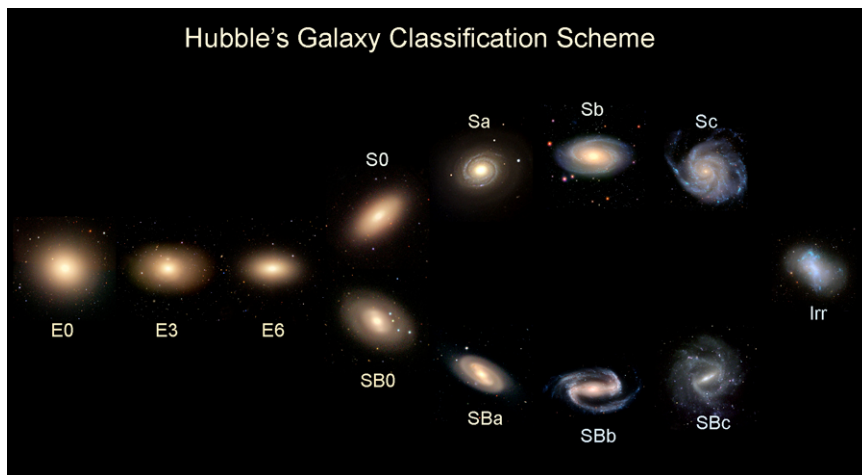Figure 1.1: **Hubble morphological classification.**

$z \simeq 0$) between *early-type* (ETGs) and *late-type* galaxies, because a strong bimodality is observed in many of their properties: colour, age of the stellar populations, star formation rate (SFR), metallicity, interstellar medium (ISM), hosting environment density and of course morphology. ETGs, which include Es and S0s and represent the subject of our

study, are typically redder, populated by older stars, passive (absent or almost absent star formation events), more metal-rich, rich of hot gas but poor of cold/warm gas and, finally, they mainly populate denser environments (galaxy groups and clusters).

These galaxies show a surface brightness profile well described by the Sérsic (1963) law:

$$I(R) = I_e \, e^{-b_n \left[\left(\frac{R}{R_e} \right)^{1/n} - 1 \right]}, \tag{1.1}$$

where $b_n = 2n - 0.324$; often, $b_n = 4$ is adopted, providing the de Vaucouleurs (1948) profile, but actually it is found that the so-called *Sersic index n* increases by increasing the total galaxy luminosity L and so it is *non-universal* for all ETGs. This correlation between n and L is only one of the relations between structural, dynamical and chemical properties of ETGs, called *Scaling Laws* (SLs). Faber and Jackson (1976) first found a relation between luminosity (total or in a given band) and stellar velocity dispersion, measured within a certain aperture radius (e.g. R_e), called *Faber-Jackson relation*: $L \propto \sigma_e^{\sim 4}$. The second relation to be discovered was between surface brightness and size: the surface brightness was measured within the effective radius, so $I_e = L/(2\pi R_e^2)$, and R_e usually is taken as reference for the galaxy size; this relation, due to Kormendy (1977), is often expressed as a *size-luminosity* relation. These two SLs represent the projections, respectively on the plane $L - \sigma_e$ and $R_e - L$, of the so-called *Fundamental Plane* (Dressler et al., 1987; Djorgovski and Davis, 1987). All ETGs lie, with a small scatter, on a plane on the space coordinates $(\log L, \log \sigma_e, \log R_e)$, which is the most important observed feature of ETGs, because it suggests a *quasi homology* in their structure. Observations of the ATLAS ^{3D} survey, through IFS (Integral-Field Spectroscopy), provided the following proportionality, shown in figure 1.2:

$$L \propto \sigma_e^{1.25} R_e^{0.96}. \tag{1.2}$$

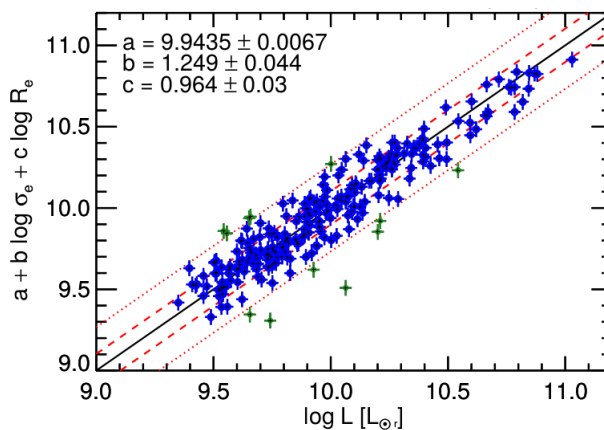Other SLs can be mentioned, for example, the *mass-metallicity* and *mass-colour* ones.

Figure 1.2: Fundamental Plane. *Edge-on* view of the Fundamental Plane observed for a sample of ETGs of the ATLAS ^{3D} survey. Here, L is in units of $L_{\odot,r}$, σ_e in units of $130 \, \mathrm{km \, s^{-1}}$ and R_e in units of 2 kpc. The figure is taken from Cappellari, Scott et al. (2013).

Overall, from these empirical relations, we note that ETGs more massive are in general brighter, larger, more metal-rich, redder, than less massive ones.

Most of ETGs host a supermassive black hole (hereafter BH) located in the galactic centre, of which only about 1% is active, i.e. only about 1% of galaxies host an AGN (Active Galactic Nucleus). Despite this is an open research field, it is widely confirmed that there is an important co-evolution of the BH and the host galaxy. Some SLs have been found, in fact, relating galaxy properties with the central BH mass. First of all, a very tight relation exists between the BH mass and the stellar velocity dispersion: $M_{BH} \propto \sigma_e^4$. Note that also the galaxy luminosity is proportional to the fourth power of σ_e (Faber-Jackson relation), thus, assuming a constant stellar mass-to-light ratio, a linear relation between the BH mass and the stellar galaxy mass is derived from Magorrian et al. (1998) and it is called *Magorrian relation*: $M_{BH} \simeq 10^{-3} M_*$.

1.2   Morphology and kinematics

ETG morphology can be approximately described by a sphere, an axisymmetric (oblate or prolate) ellipsoid or a triaxial ellipsoid. When projected on the sky, they appear as ellipticals (or circles), so the observed ellipticity is given by the ratio between minor and major axes, $\varepsilon = 1 - b/a$. This value usually varies from 0 (E0) up to 0.7 (E7), that represents the maximum flattening of observed elliptical galaxies. In our study, we consider galaxies as stellar systems in equilibrium, where the shape is mainly due to the stellar rotation velocity (ordered motion) or to the anisotropy of the stellar velocity dispersion tensor (random motion). In general, the support is due to a combination of these effects, producing anisotropic rotators, while the limit cases are represented by the isotropic rotator (rotationally supported system) and by the non-rotating system, fully supported by the anisotropy. Binney (1978) first proposed the so-called $(v/\sigma, \varepsilon)$ diagram, as a theoretical plane, derived from the tensor Virial Theorem, showing the relation between dynamical and morphological properties of elliptical galaxies, as a function of their anisotropy. In particular, it represents the dependence of the ratio between the rotation velocity and the velocity dispersion on the ellipticity, for different degrees of anisotropy. The anisotropy is given by the non-negative parameter $\delta = 1 - \Pi_{zz}/\Pi_{xx}$, where Π_{zz} is the component along the z-axis of the random kinetic energy tensor, while Π_{xx} is in a direction orthogonal to it. In figure 1.3, the $(v/\sigma, \varepsilon)$ diagram is shown, comparing observations of Davies et al. (1983) with recent observations, made possible since the advent of the IFS (Emsellem et al., 2011; Cappellari, 2016). In both versions, the line representing isotropic rotators ($\delta = 0$) is shown, under the assumption of axisymmetric oblate spheroids, with ordered rotation only around the z-axis. For galaxies lying on this line (the upper one in Cappellari diagram), the ratio v/σ is unambiguously determined by the ellipticity. While, in the opposite case of non-rotating system ($v = 0$), the anisotropy is unambiguously determined by the ellipticity. Instead, in the general case of anisotropic rotator ($\delta > 0$, $v > 0$), there is a degeneracy on the $(v/\sigma, \varepsilon)$ plane: a certain degree of flattening can be obtained by different contributions of the rotation velocity and the anisotropy. Note that the limit case of spherical galaxy is consistent only with
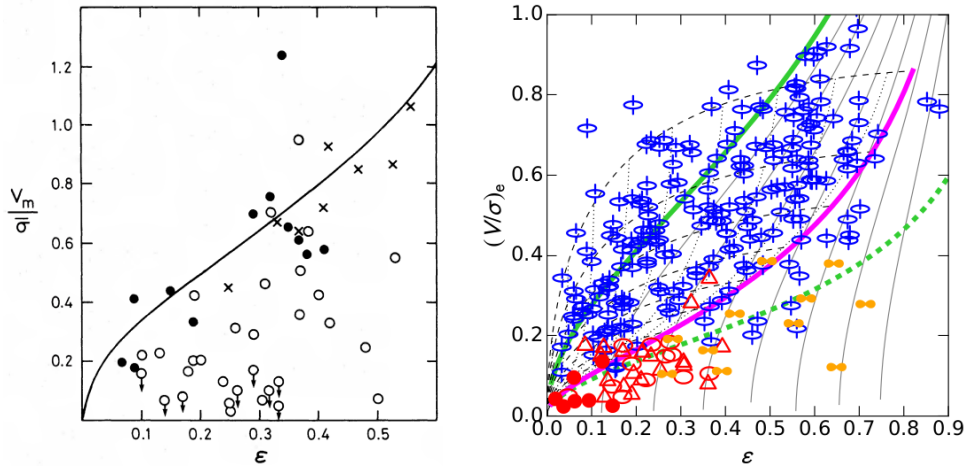
Figure 1.3: **(v/σ, ε) diagram.** The figure on the left is taken from Davies et al. (1983), while that on the right shows observations of the ATLAS [3D] survey of Emsellem et al. (2011), as reported in the review of Cappellari (2016). See the text for details about all features shown.

the isotropic non-rotating system, located in the origin of the plane. In Cappellari diagram, grey lines correspond to increasing anisotropy, separated by $\Delta\delta = 0.1$. Note that, since ε is the observed ellipticity, the intrinsic one, ε_{intr}, is equal to ε in case of galaxy seen edge-on, but decreases with respect to ε, by decreasing the inclination, following the grey dashed lines. The magenta and the green dotted lines represent specific values of δ, which distinguish the behaviour of different kinematic types of ETGs, plotted with different symbols (see Cappellari, 2016, for more details). Few words have to be spent about the plotted ratio v/σ. In the original theoretical plane proposed by Binney (1978), v and σ derive from the integration from 0 up to ∞ of the ordered and random kinetic energy tensor, respectively; when galaxies are observed, instead, measures are taken within a limited radius. Davies et al. plotted the maximum rotation velocity of each galaxy, v_m, on the average velocity dispersion measured within $R_e/2$, called $\bar{\sigma}$; while Cappellari plotted the luminosity-weighted ratio within R_e. In both cases, however, the measured ratio is very close to the theoretical one, extended to infinite radii.

1.3 Dark matter and stellar populations: dynamical and population synthesis models

ETGs are multi-component systems, composed by stars, interstellar medium (ISM), a supermassive black hole and dark matter (DM). The stellar component, of which we have already introduced some properties and which dominates the total galaxy luminosity, can vary in mass from about $10^9 - 10^{10}\, M_\odot$ up to $10^{12}\, M_\odot$ for Es and S0s and from about $10^7\, M_\odot$ up to $10^9 - 10^{10}\, M_\odot$ for dwarf spheroids, that are usually included in ETGs. In figure 1.4, the mass-size distribution of a large sample of galaxies is shown: this is not representative of all observable galaxies, but it is quite illustrative of their stellar mass
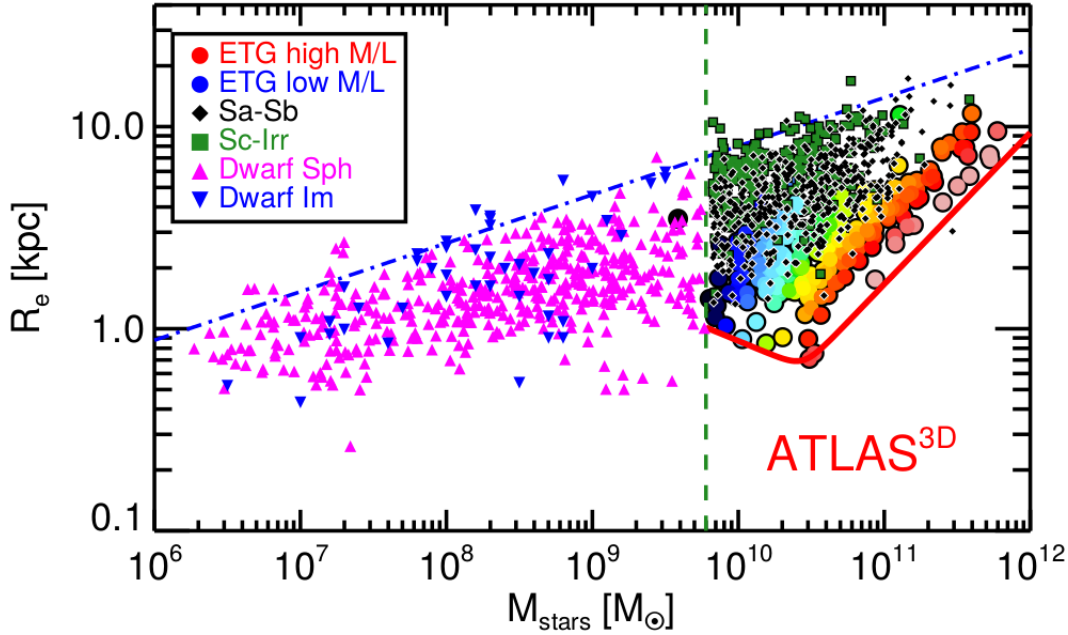
Figure 1.4: Mass-size distribution. The figure is taken from Cappellari, McDermid et al. (2013), to which the reader is referred for details about all features shown.

and size ranges. In most of ETGs, a central supermassive BH is also present, with mass three orders of magnitude less than the stellar one (Magorrian et al., 1998), as introduced in section 1.1. The ISM, mainly including gas and dust, can reach a mass of about two orders of magnitude less than the stellar mass; since its gravitational contribution is negligible for the global stellar dynamics, so it is not considered in dynamical galaxy models, we do not discuss it any further. A relevant matter component is, instead, the dark matter: we do not know much about its nature and distribution, but over the past few decades many evidences have been reported about its existence in galaxies. Cosmological numerical simulations suggest that it is isotropically distributed in a halo, more extended than the stellar galaxy, and it can reach a mass up to about two orders of magnitude greater than the stellar mass.

Building dynamical galaxy models allows to give an interpretation of the observed structure and kinematics and to quantify non-observable features, like the dark matter amount and stellar population properties, which represent the subject of our study. A general assumption of dynamical models is that galaxies are systems in equilibrium, with a simple spherical, axisymmetric or triaxial shape. A method of dynamical modelling, but not the only one, is that based on the solution of the Jeans equations, so-called because they have been applied to the stellar dynamics for the first time by Jeans (1922). Numerical codes based on this method are, for example, JAM (Jeans Anisotropic Modelling), developed by Cappellari (2008), and JASMINE (Jeans AxiSymmetric Models of galaxies IN Equilibrium), developed by Posacki et al. (2013), on which we based our study. Different works, based on Jeans models of large samples of ETGs (e.g. Cappellari,

Scott et al. (2013); Posacki et al. (2015); Poci et al. (2017)), where the DM component is modelled by *cosmologically-motivated* halos, found a median DM fraction less than about 20%. This quantity represents the ratio between the DM mass and the total mass within a sphere of radius R_e, thus this small value means that the amount of DM in the inner region of galaxies is considerably lower than the total matter. For each galaxy model, the stellar mass-to-light ratio, assumed to be constant with radius, can be computed and used for a comparison with values inferred from evolutionary population synthesis (EPS) models: usually they are called $(M_*/L)_{dyn}$ and $(M_*/L)_{pop}$, respectively. The EPS is the technique of modelling the spectrophotometric properties of stellar populations, based on the knowledge of the evolution of stars and on the assumption of a constant stellar initial mass function (IMF), which describes the distribution of the stellar masses when the population formed (e.g. Maraston, 2005, for reference). Nevertheless, a discrepancy between these mass-to-light ratios is discovered, when $(M_*/L)_{pop}$ are derived by assuming the original Salpeter (1955) IMF, as can be seen e.g. in figure 1.5, as a function of the stellar velocity dispersion observed within R_e, for dynamical models of the ATLAS [3D] and SLACS galaxies. In particular, $(M_*/L)_{dyn}$ is lower than $(M_*/L)_{pop}^{Salp}$ for galaxies with
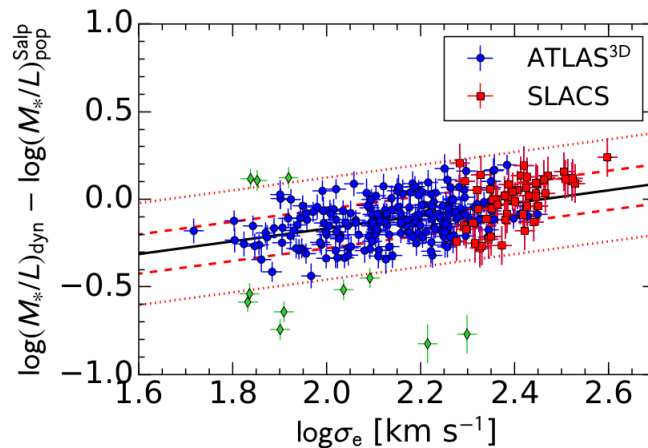

Figure 1.5: IMF-σ relation. The ratio between the stellar mass-to-light ratios inferred from dynamical models and from stellar population models, assuming a Salpeter IMF (1955), is shown as a function of the stellar velocity dispersion observed within R_e, for galaxies from the ATLAS [3D] and SLACS surveys, in logarithmic scale. When the y-value is zero, $(M_*/L)_{dyn} = (M_*/L)_{pop}^{Salp}$. The figure is taken from Cappellari (2016), to which the reader is referred for details about all features shown.

low σ_e and the discrepancy decreases with visible regularity by increasing the velocity dispersion. This suggested that a systematic variation of the DM fraction or IMF, as a function of the velocity dispersion, is required. In other words, the DM fraction and the stellar IMF cannot be both *universal* in ETGs. Actually, dynamical models of ETGs of the ATLAS [3D] sample showed that the discrepancy cannot be explained by a variation of the DM fraction, obtained by varying the DM profile with respect to the original NFW one (Navarro et al., 1996). Therefore, a systematic variation of the IMF seems to be necessary, as summarised in Cappellari et al. (2012), suggesting the *non-universality* of

the IMF in ETGs. Overall, the systematic trend in the discrepancy between $(M_*/L)_{dyn}$ and $(M_*/L)_{pop}^{Salp}$ is solved by assuming an IMF with a "lighter" slope at low stellar masses with respect to the original Salpeter IMF, for example the Kroupa (2001) IMF; while, as the galaxy mass increases, the Salpeter IMF describes increasingly well the distribution of the stellar masses when the population formed in ETGs. A large number of stars with low mass, in fact, produces a large mass-to-light ratio, since they count on the total mass but very little on the total luminosity.

1.4   Overview of this thesis

In this thesis work, we intend to study ETGs from a dynamical point of view, in order to investigate the DM amount and distribution, in relation to the stellar properties, constrained by observations of the kinematic field of galaxies. This is accomplished by using the original numerical code JASMINE, developed to build dynamical models of ETGs, based on the solution of the Jeans equations. The code is developed and tested to produce axisymmetric (oblate) galaxy models, rotating around the axis of symmetry and with anisotropic stellar orbits.

In chapter 2, we give a description of our Jeans models, composed of three components of matter (stars, BH and DM). In chapter 3, we show the results of the code, from the density and mass profiles of both stellar and DM distributions, to the stellar velocity dispersion profiles due to the gravitational contribution of each component of matter, focusing on the effects of the stellar and DM structural parameters. We also report a robustness test of the code, accomplished by making a comparison between numerical and analytical solutions of the Jeans equations, for specific models. Then, we report a test of our models, by making a comparison between the DM fractions, inferred from the JASMINE models and from dynamical models of a large sample of observed ETGs. Chapter 4 is focused on the main results achieved from this thesis work. First, we investigate how much "freedom" observations in the central region of ETGs allow about the DM structure. For this purpose, we model the DM component by the well known NFW profile and we adopt, for the stellar component, values of the mass-to-light ratio derived from EPS models. Then, we explore the effect of a different DM distribution, with a "torus-like" shape, located in the outer region of galaxies, on the projected central velocity dispersion of stars. Finally, in chapter 5, we conclude this thesis work with the discussion of the results and a look at the future prospects. Appendix A and B are focused on a brief technical description of the Jeans equations and the JASMINE code, respectively.

Enjoy the reading!

Chapter 2

Models

In this chapter, we describe the galaxy modelling employed in our study, from a theoretical point of view. We build three-component ETG models composed of stars, dark matter (DM) and a central supermassive black hole (BH). This latter is the most simple gravitational contribution ans it is described first; while the next two sections, 2.1 and 2.2, are dedicated to the stellar and DM distributions, respectively. Although, in this thesis work, we focus on spherically symmetric galaxy models, we prepare the code to build models with a more general axisymmetric stellar distribution: in particular, it is an oblate spheroid with minor axis aligned with z-axis, thus it is convenient to employ cylindrical coordinates (R, φ, z). The DM component is instead modelled by a spherical halo, more extended than the stellar galaxy. In section 2.3, we explain how we derive the stellar and halo parameters, starting from the Scaling Laws. Finally, in section 2.4, we briefly discuss about flattening spherical galaxy models.

The BH mass M_{BH} derives from the Magorrian et al. (1998) relation ($M_{BH} = 10^{-3} M_*$) and it is treated as a point mass at the centre of the galaxy, producing the isotropic gravitational potential

$$\phi_{BH}(r) = -\frac{GM_{BH}}{r}, \tag{2.1}$$

where $r = \sqrt{R^2 + z^2}$ is the spherical radius. The radial and vertical gravitational accelerations, i.e. the opposites of the gradients of the potential along the R and z axis respectively, are given by:

$$f_{R,BH}(R, z) = -\frac{\partial \phi_{BH}}{\partial R} = -\frac{GM_{BH}}{r^3} R, \tag{2.2}$$

$$f_{z,BH}(R, z) = -\frac{\partial \phi_{BH}}{\partial z} = -\frac{GM_{BH}}{r^3} z.$$

Hereafter the accelerations will often be called *forces*, implying that they are forces per unit mass.

2.1   Stellar distribution

The axisymmetric stellar distribution is characterised by a certain degree of flattening, specified by the choice of the ratio $q = b/a$ between the minor and major axis of the spheroid. The reader is referred to section 2.4 for a detailed treatment of the flattening technique employed. The calculation of the total stellar mass M_* is described in section 2.3. We consider two different axisymmetric density profiles: the deprojected de Vaucouleurs and the Jaffe ones.

For the de Vaucouleurs (1948) surface brightness profile ("$R^{1/4}$ ")

$$I(R) = I_e \, e^{-7.67\left[\left(\frac{R}{R_e}\right)^{1/4}-1\right]}, \tag{2.3}$$

the corresponding density profile $\rho_*(R, z)$ is obtained from the deprojection of Mellier and Mathez (1987), that is a useful analytical approximation of the Abel inversion formula:

$$\rho_*(R, z) = \rho_0 \xi^{-0.855} e^{-\xi^{1/4}}, \tag{2.4}$$

where

$$\rho_0 = \frac{M_* b_n^{12}}{16\pi q R_{e0}^3 \Gamma(8.58)}, \qquad \xi = \frac{b_n^4}{R_{e0}}\sqrt{R^2 + \frac{z^2}{q^2}}. \tag{2.5}$$

Here $b_n = 2n - 0.324 \simeq 7.67$, as for the Sersic law with index $n = 4$ (the Sérsic (1963) law of is in fact a generalization of the de Vaucouleurs law). R_{e0} is the *circularized* effective radius, i.e. the effective radius when the galaxy is seen face-on (FO). The effective radius is indeed a projected quantity, which represents the geometric mean of the major and minor axis of the elliptical isophote containing half of the total luminosity of the galaxy, called ellipse of *half-light* (or simply the radius of the circular isophote of half-light). The projected effective radius when the galaxy is seen edge-on (EO) is $R_e = R_{e0}\sqrt{q}$; obviously it is equal to R_{e0} in case of FO view of a flat galaxy or in case of any view of a spherical galaxy.

The Jaffe (1983) profile of an ellipsoidal density distribution is

$$\rho_*(R, z) = \frac{M_*}{4\pi r_*^3 m^2 (1 + m)^2}, \tag{2.6}$$

where

$$m^2 = \frac{R^2}{r_*^2} + \frac{z^2}{q^2 r_*^2} \tag{2.7}$$

and

$$r_* \simeq \frac{4}{3} R_e, \tag{2.8}$$

which is an approximate relation between the Jaffe scale radius r_* and the effective radius R_e; it was found by Jaffe in his original work and recently by Ciotti and Ziaee Lorzad (2018), with a negligible difference.

2.2 Dark matter distribution

We model the DM distribution with an isotropic NFW profile (Navarro et al., 1996), truncated at a radius r_t, as follows:

$$\rho_h(r) = \frac{M_h}{4\pi r(r + r_h)^2 f(c)}. \tag{2.9}$$

Here M_h is the halo mass within r_t; r_h is the scale radius of the NFW profile, which we relate to the effective radius of the stellar component by introducing the parameter $\beta \equiv r_h/R_e$; $c = r_t/r_h$ is the concentration parameter, which enters in the NFW profile through the function $f(c) = \ln(1+c) - \frac{c}{1+c}$. [1] The gravitational potential and the radial and vertical forces due to this component are

$$\phi_h(r) = -\frac{GM_h}{f(c)} \frac{\ln\left(1 + \frac{r}{r_h}\right)}{r}, \tag{2.10}$$

$$f_{R,h}(R, z) = \frac{GM_h}{f(c)} \left[-\ln\left(1 + \frac{r}{r_h}\right) + \frac{r}{r + r_h} \right] \frac{R}{r^3}, \tag{2.11}$$

$$f_{z,h}(R, z) = \frac{GM_h}{f(c)} \left[-\ln\left(1 + \frac{r}{r_h}\right) + \frac{r}{r + r_h} \right] \frac{z}{r^3}.$$

By definition, the DM halo is extended up to r_t, therefore beyond this radius the DM density is zero and the potential and the forces become:

$$\phi_h(r) = -\frac{GM_h}{r}, \tag{2.12}$$

$$f_{R,h}(R, z) = -\frac{GM_h}{r^3} R, \qquad f_{z,h}(R, z) = -\frac{GM_h}{r^3} z. \tag{2.13}$$

For some tests, we also consider an additional component of DM, that we call *external* DM distribution: it is described by a simple gaussian function, centred at a given radius r_0, chosen in the region where the NFW profile decreases as r^{-3}, which means between r_h and r_t. The radial density profile of this isotropic distribution is

$$\rho_{ext}(r) = a\, e^{-\frac{(r-r_0)^2}{2b^2}}, \tag{2.14}$$

where we take for the position of the peak $r_0 = r_t/2$ and for the standard deviation $b = r_h$, reminding that $r_h = \beta\, R_e = r_t/c$. The normalisation constant a is fixed through

---

[1]Since Navarro, Frenk and White (Navarro et al., 1996) obtained this density profile for the DM halo from cosmological N-body simulations, we briefly give their definitions of the parameters, based on the formation theory of CDM halos through the growth of density perturbations in an expanding Universe. The truncation radius represents the virial radius r_{200}, within which the mean density of the halo is about $200\rho_{crit}$, where $\rho_{crit} = \frac{3H^2}{8\pi G}$ is the critical density of the Universe at the redshift of formation. The total mass of the halo is defined as the mass enclosed within r_{200}, so $M_{200} = \frac{4\pi}{3} r_{200}^3\, 200\rho_{crit}$.

the choice of a value for the total mass of this distribution, M_{ext}, by requiring that $4\pi \int_0^\infty \rho_{ext}(r)r^2 dr = M_{ext}$, so

$$
\begin{aligned}
M_{ext} &= 4\pi a \int_0^\infty e^{-\frac{(r-r_0)^2}{2b^2}} r^2 dr = \\
&= 2\pi ab \left\{ \sqrt{2\pi}(b^2 + r_0^2)\left[1 + erf\left(\frac{r_0}{\sqrt{2}b}\right)\right] + 2br_0 e^{-\frac{r_0^2}{2b^2}} \right\}
\end{aligned}
\tag{2.15}
$$

and then

$$
a = \frac{M_{ext}}{2\pi b \left\{ \sqrt{2\pi}(b^2 + r_0^2)\left[1 + erf\left(\frac{r_0}{\sqrt{2}b}\right)\right] + 2br_0 e^{-\frac{r_0^2}{2b^2}} \right\}}.
\tag{2.16}
$$

The gravitational accelerations due to this distribution are

$$
f_{R,ext}(R,z) = -\frac{GM_{ext}(r)}{r^3}R, \qquad f_{z,ext}(R,z) = -\frac{GM_{ext}(r)}{r^3}z,
\tag{2.17}
$$

with $M_{ext}(r)$ calculated from the analytical integration of the density between 0 and r, once a is fixed:

$$
\begin{aligned}
M_{ext}(r) &= \int_0^r \rho_{ext}(r')r'^2 dr' = \\
&= 2\pi ab \left\{ \sqrt{2\pi}(b^2 + r_0^2)\left[erf\left(\frac{r-r_0}{\sqrt{2}b}\right) + erf\left(\frac{r_0}{\sqrt{2}b}\right)\right] \right. \\
&\quad \left. - 2b\left[(r+r_0)e^{-\frac{(r-r_0)^2}{2b^2}} - r_0 e^{-\frac{r_0^2}{2b^2}}\right] \right\}.
\end{aligned}
\tag{2.18}
$$

2.3 Realistic models

Real ETGs satisfy some Scaling Laws (SLs), thus our models have to reproduce these empirical relations to be realistic. We consider the two most important of these SLs: the Faber-Jackson and the size-luminosity relations, between $\sigma_{e8} - L_r$ and $L_r - R_e$ respectively, as derived for a sample of about 80 000 ETGs from Data Release 4 of the SDSS (Desroches et al., 2007):

$$
\log \sigma_{e8} = -1.79 + 0.674 \log L_r - 0.0234 \log^2 L_r,
\tag{2.19}
$$

$$
\log R_e = 1.50 - 0.802 \log L_r + 0.0805 \log^2 L_r.
\tag{2.20}
$$

Here σ_{e8} is the central luminosity-weighted velocity dispersion of the stars (within the projected radius $R_e/8$, which represents a very central region) in units of $\mathrm{km\,s^{-1}}$; L_r is the total luminosity in the r band, calibrated to the AB system; R_e is the effective radius in units of kpc.

We first build spherical models with different values of σ_{e8}, called *progenitors*, which

satisfy these relations, and then we flatten them: from each progenitor, we obtain a *family* of galaxies with different degrees of flattening, as described in section 2.4 below. After calculating L_r for a given σ_{e8} using eq. (2.19), we convert it to the V band luminosity L_V, with the appropriate transformation equation (Jester et al., 2005) between SDSS magnitudes and other systems $[M_V = M_r - 0.11 + 0.42(B - V)]$, assuming $B - V = 0.9$; then R_e is calculated from eq. (2.20). The halo scale radius is consequently derived, by fixing a value for β, so $r_h = \beta R_e$; thus, the truncation radius is computed, by fixing a value for c, so $r_t = c\, r_h$. Note that when the Jeans equations are solved (see appendix A and B), the resulting stellar velocity dispersion is given by the sum of the gravitational contributions of the stars themselves, BH and DM, for certain values of stellar mass and halo mass; in order for the model to be consistent with the SLs, its computed projected central velocity dispersion has to reproduce the chosen value for σ_{e8} satisfying the SLs. We can therefore obtain the stellar mass in two ways, physically different: fixing the mass-to-light ratio or reproducing the given σ_{e8}. In any case the stellar mass-to-light ratio in the V band $(\Upsilon_{*\,dyn} \equiv M_*/L_V)$ [2] is assumed to be constant with radius. In the first case, we choose an a priori value appropriate for a 12 Gyr old stellar population, with solar metallicity and a Kroupa IMF (see Maraston, 2005, for reference); then M_* is derived, as shown schematically in figure 2.1. That means the stellar component is fixed, while M_h is calculated to reproduce σ_{e8}. In the second and more flexible case, both M_* and M_h are calculated a posteriori, by varying their contributions in order to reproduce σ_{e8}. This latter and more complicated case is fully analysed in section 4.1 and schematically illustrated in figure 4.1; in section 3.4, it is also explained why we can avoid to fix the concentration parameter c of the NFW DM halo and keep it as a free parameter, together with M_h.
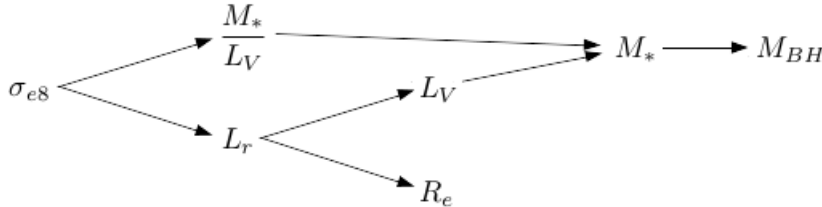
Figure 2.1: Diagram with fixed mass-to-light ratio. How stellar properties are derived from the input σ_{e8}, by fixing $\Upsilon_{*\,dyn} \equiv \frac{M_*}{L_V}$.

2.4 Flattening spherical models

For details about the technique employed to flat spherical galaxy models and the effect of flattening on their structural and dynamical properties, see Posacki et al. (2013) or

---

[2]In agreement with other works (e.g. Cappellari et al., 2012; Cappellari, 2016) we call $\Upsilon_{*\,dyn}$ the mass-to-light ratio inferred from dynamical models, to distinguish it from the mass-to-light ratio derived from Simple Stellar Population synthesis models, which we call $\Upsilon_{*\,pop}$.

Posacki (2014); here we avoid to go deeply into these points, because it is over the matter of this thesis work, since we are not studying flat models. Nevertheless, since the code is ready to build also flat galaxy models and this is in our plan for the future, we give a brief explanation of the technique of flattening and on its effect.

For simplicity, we consider only two possible inclinations of the z-axis with respect to the line of sight (l.o.s.) direction: $0°$ and $90°$, that correspond to the FO-view and the EO-view respectively. Thus the spherical progenitor ($q = 1$) can be flattened in two different ways, always keeping R_e constant, and it produces two *sub-families* of models called "FO-built" ones and "EO-built" ones, each model characterised by a different degree of flattening ($0.3 \leq q < 1$). In the first case, the progenitor is compressed along the z-axis and the flat model keeps the original R_e when it is seen FO; in the other case, the oblate spheroid is obtained expanding the progenitor on the galactic plane, so R_e does not change in case of EO-view. The SLs are resolved with a certain value of σ_{e8}, thus all models of the same family have the same L in each band, in addition to the same observed R_e. The DM distribution is totally unchanged with the flattening, since we assume a spherical DM halo also in case of a flat stellar component. After the resolution of the Jeans equations for a flat model, the computed σ_{e8} is less than that of the progenitor, i.e. the one satisfying the SLs, because of the effect of flattening on the galaxy model.

Chapter 3

Code tests

In this chapter, we illustrate some of the tests we have done, by exploiting the original numerical code JASMINE, described in appendix B. It has already been widely tested over the past few years: e.g. by comparing the numerical solutions with the analytical solutions of the Jeans equations (JEs) known for two-component axisymmetric galaxy models, made of a Miyamoto-Nagai disc embedded in a Binney logarithmic potential (Posacki, 2014); it has also been tested against another Jeans solver code, JAM (Jeans Anisotropic Modelling), developed by Cappellari (2008), which builds dynamical axisymmetric models for the SLACS sample of ETGs (Posacki, 2014; Posacki et al., 2015).

In section 3.1, we illustrate the stellar models produced by the code. Although, as shown in the previous chapter, the code is developed to build more general axisymmetric (oblate) anisotropic galaxy models, in this thesis work we study spherical isotropic ones, with two possible stellar profiles (deprojected de Vaucouleurs or Jaffe) and a central supermassive black hole (BH), with mass related to the total stellar mass by the Magorrian et al. (1998) relation. In section 3.2, we illustrate, instead, the modelling of the dark matter (DM) component, described by a spherical NFW profile and we give a robustness test of the code against analytical models. In section 3.3, we analyse the dependence of the halo mass, enclosed in the total galaxy and within the effective radius, on the stellar and halo parameters; in particular, we analyse the dark matter fractions inferred from our dynamical models and we compare them with those from other dynamical models based on the observations of large samples of ETGs. Finally, in section 3.4, we show that the position of the truncation radius of the NFW halo does not affect the dynamics of stars in a region central enough, allowing the more flexible modelling presented in the next chapter.

3.1   Stellar distribution

In this section, we analyse the stellar component modelling of spherical galaxies, with isotropic stellar orbits, taking as examples models with projected central velocity disper-

q	k	σ_{e8} (km s^{-1})	$\Upsilon_{*dyn} \equiv \frac{M_*}{L_V}$	R_e (kpc)	$L_{V10} \equiv \frac{L_V}{10^{10} L_\odot}$	$M_{*10} \equiv \frac{M_*}{10^{10} M_\odot}$
1	1	180	3.62	3.26	2.23	8.10

Table 3.1: **Stellar properties of the deprojected de Vaucouleurs and Jaffe models.** Both models are spherical ($q = 1$) and with isotropic stellar orbits ($k = 1$ from the Satoh (1980) decomposition, appendix B), with the same projected central velocity dispersion σ_{e8}, mass-to-light ratio Υ_{*dyn}, effective radius R_e, luminosity L_{V10} and stellar mass M_{*10} (from left to right).

sion $\sigma_{e8} = 180 \, \text{km s}^{-1}$. As introduced in section 2.3 and defined in appendix B (eq. B.18), σ_{e8} is the luminosity-weighted velocity dispersion of stars, within an aperture radius of $R_e/8$, taken as *central* radius. In this thesis work, we consider two density profiles for modelling the stellar distribution: the deprojected de Vaucouleurs and the Jaffe ones. Their density profiles are given in section 2.1 (eqs. 2.4 and 2.6, respectively), in the axisymmetric form, so that the code is ready to build also axisymmetric (oblate) ellipsoid; while the mass profile is numerically computed and the velocity dispersion one is obtained from the solution of the vertical JE. We assume spherical symmetry and fully isotropic velocity dispersion tensor, so we show the *radial* profiles for a de Vaucouleurs and a Jaffe stellar distribution, in order to illustrate what the code produces; we also compare them to show their similarities and differences. The two models compared have the same projected central velocity dispersion $\sigma_{e8} = 180 \, \text{km s}^{-1}$, so the effective radius and luminosity derived trough the SLs (section 2.3) are equal too. The mass-to-light ratio $M_*/L_V \equiv \Upsilon_{*dyn} = 3.62$ is fixed according to Maraston (2005), as illustrate in section 2.3 and in figure 4.1; the total stellar mass is finally computed. These values are summarised in table 3.1.

In fig. 3.1, the density profiles of both distributions are shown: although the Jaffe one is higher in the inner and outer regions, while the de Vaucouleurs one is only weakly higher in the medium region, the total stellar masses contained in these galaxies are equal. In fact, the inner region, though very dense, represents a very small volume and the outer region, even if very large, contains very low mass; overall, the mass contained in the de Vaucouleurs profile equals that of the Jaffe one. In fact, as visible in fig. 3.2, the cumulative mass of the de Vaucouleurs model is lower at inner radius and then it reaches the Jaffe one. The relative positions of the effective radius reflect this difference: the *half-light* radius of the Jaffe profile is less than the de Vaucouleurs one.

The figure 3.3 shows the stellar velocity dispersion profiles of both models, as the sum of the stellar and BH gravitational contributions. In order to see better the role of the central supermassive BH, in this case, the scale is extended down to $r = 10 \, pc$. In fact, the BH increases significantly the total velocity dispersion only in a very inner region, while above 100 pc its contribution is almost negligible. It is relevant to note that the Jaffe profile, for the same Υ_{*dyn}, produces a greater velocity dispersion at $R_e/8$ (and so a greater projected central velocity dispersion σ_{e8}). It means that, in general, a model with Jaffe stellar distribution requires less DM to reproduce σ_{e8}. We will explore further
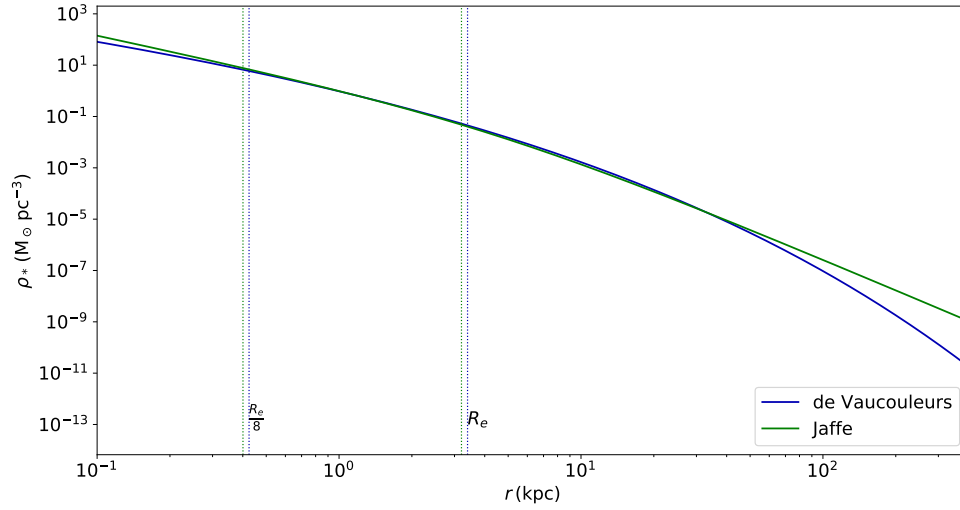
Figure 3.1: Density profiles. Deprojected de Vaucouleurs (blue) and Jaffe (green) models, with stellar properties given in table 3.1. The vertical lines represent the effective radius R_e and the *central* radius $R_e/8$ for each profile.
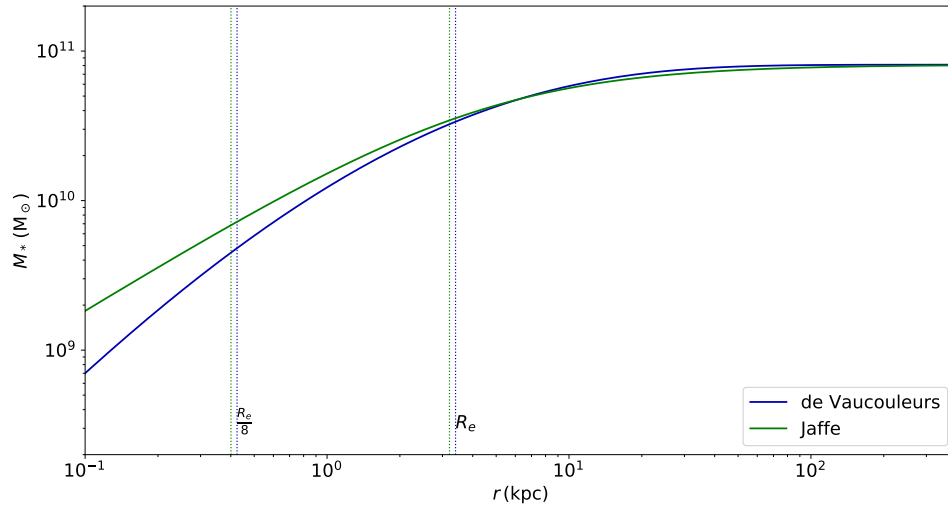

Figure 3.2: Mass profiles. Deprojected de Vaucouleurs (blue) and Jaffe (green) models of fig. 3.1, with stellar properties given in table 3.1.
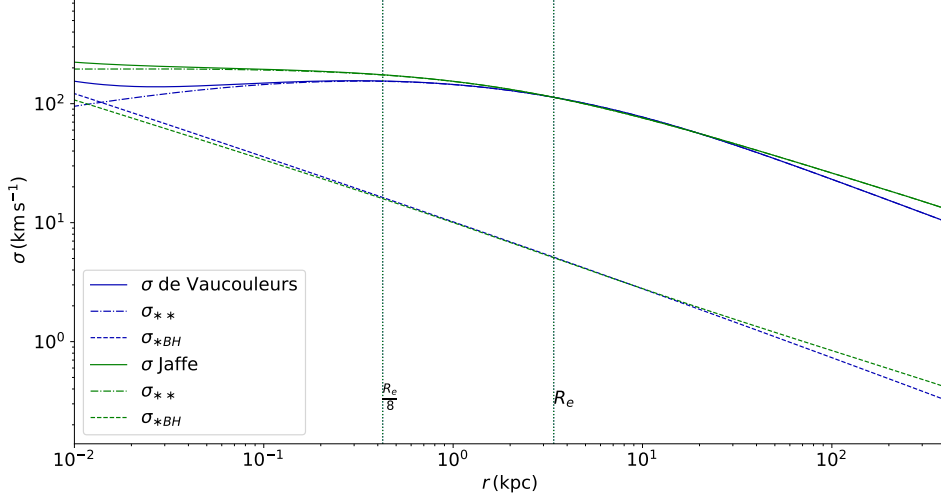
Figure 3.3: Velocity dispersion profiles. Deprojected de Vaucouleurs (blue) and Jaffe (green) models of fig. 3.1, with stellar properties given in table 3.1. They are the sum of the stellar and BH contributions (σ_{**} and σ_{*BH}, respectively), between 10 pc and 400 kpc, to show better the role of the central BH.

this point in the next sections.

Overall, the de Vaucouleurs and Jaffe models are quite similar and we will use both in our study. Since the Jaffe one is analytically simpler and better studied, we will often prefer to employ it, e.g. in section 4.1; while in section 4.2, the de Vaucouleurs one is used. In the next section, we discuss the inclusion of the DM component in our galaxy models.

3.2 Dark matter distribution

A galaxy model with the deprojected de Vaucouleurs stellar density profile and fixed mass-to-light ratio, as reported in table 3.1, requires a certain amount of dark matter (DM) to reproduce the chosen value for the projected central velocity dispersion σ_{e8}. This means that stars and central BH alone produce a projected stellar velocity dispersion within $R_e/8$ not high enough to equal the chosen σ_{e8}. We describe this DM distribution as a truncated NFW profile (detailed in section 2.2), by fixing the halo-to-stellar scale radius ratio $\beta \equiv r_h/R_e$ and the concentration parameter (truncation-to-scale radius ratio) $c \equiv r_t/r_h$. The concentration enters in the NFW profile through the function

$$f(c) = \ln(1+c) - \frac{c}{1+c}, \tag{3.1}$$

shown in figure 3.4, that increases slowly with c. In analogy with the previous section, we also show the density and mass profiles (figs. 3.6 and 3.5, respectively) and the
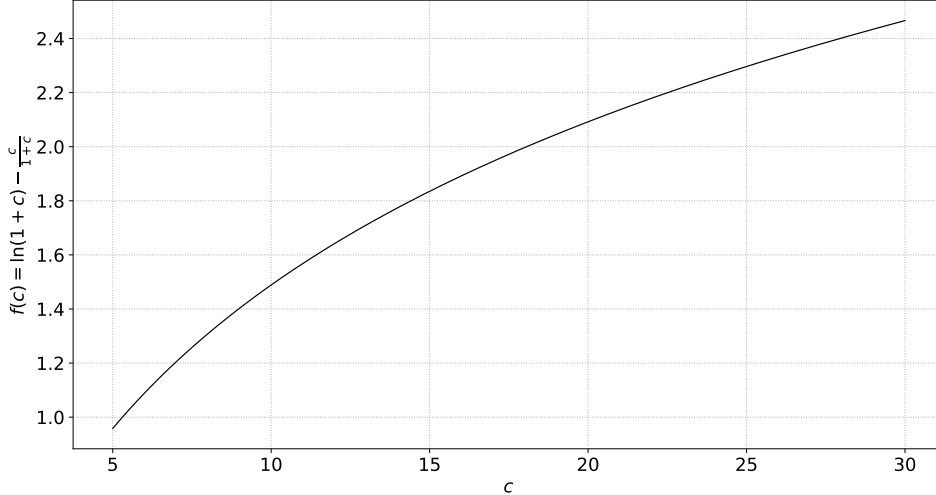
Figure 3.4: Dependence of $f(c)$ on c. The function is shown for a large range of c, corresponding to the c values we will use in the following tests.

stellar velocity dispersion profile (fig. 3.7), due to the gravitational contribution of each component (stars, BH, DM). The galaxy model has the same stellar component of the de Vaucouleurs model of the previous section, shown in figures 3.1, 3.2, 3.3 and with stellar properties given in table 3.1. Now, we fix $\beta = 7$ and $c = 10$, only to show the role of the DM halo in the galaxy model; to reproduce the given σ_{e8}, this model requires a NFW halo with mass $M_h = 1.04 \cdot 10^{13} \, M_\odot$.

In figures 3.5 and 3.6, the density and cumulative mass profiles are respectively shown. In the first one, we indicate the influence of β and c on modifying the positions of r_h and r_t; this latter, as well visible in the second figure, is the radius containing the total halo mass. The code, for a stellar effective radius R_e derived from the SLs, calculates the halo scale radius, as $r_h = \beta \, R_e$, and then the truncation radius, as $r_t = c \, r_h$. Thus, for fixed R_e, as β increases, r_h moves towards larger radii, extending the region where the density $\rho_h \propto r^{-1}$. Once r_h is fixed, as c increases, also r_t increases, producing halos more extended. It is natural that, if one did not fix a value for β and, instead, fixed r_t, by increasing c, more concentrated halos would be produced, moving r_h towards inner radii. In the next section (3.3), we will discuss the effect of β and c on the DM amount required and its fraction with respect to the stellar or total mass.

In figure 3.7, we show the total velocity dispersion profile and the contributions of the stellar component, BH and DM halo. As seen in the previous section (fig. 3.3), in the very central region, within about 10 pc from the centre, it is the BH that mainly determines the dynamics of stars; between about 10 pc and 1 kpc, the self-gravity of stars dominates; in the outer region, above about 1 kpc, the stellar contribution decreases and the halo contribution becomes dominant. The latter is, in fact, responsible for the stellar
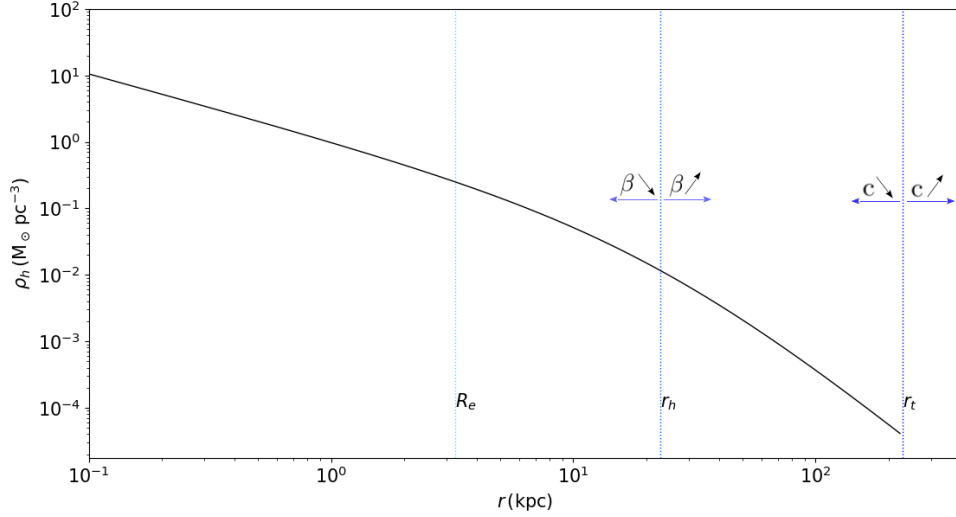
Figure 3.5: Density profile of the DM NFW halo. The scale radius r_h and the truncation radius r_t are obtained by fixing β and c, in addition to the stellar model. For this model, $\beta = 7$, $c = 10$ and the total halo mass is $M_h = 1.04 \cdot 10^{13}\, M_\odot$. For details about the stellar component of this model, see section 3.1.
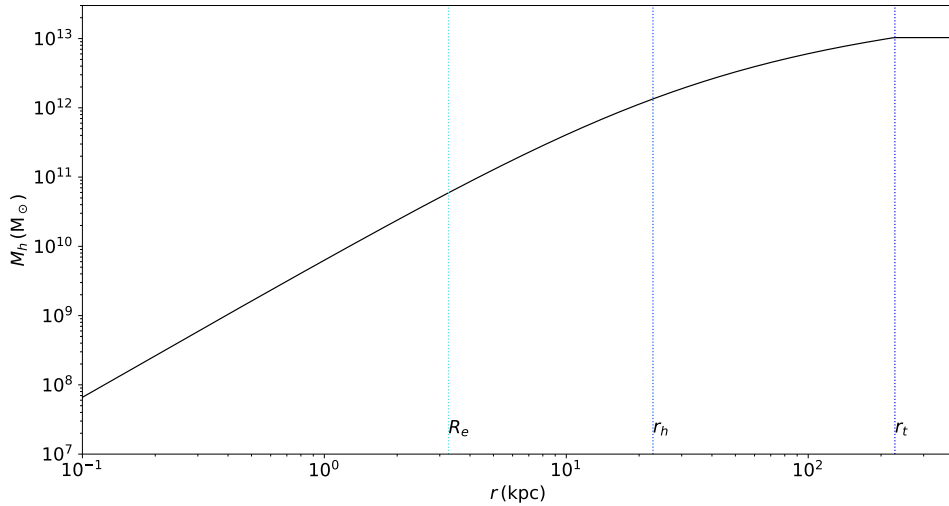
Figure 3.6: Mass profile of the DM NFW halo. The cumulative mass profile is obtained by integrating the mass density of the NFW halo. The total halo mass, $M_h = 1.04 \cdot 10^{13}\, M_\odot$, is contained within r_t; for details about the halo parameters and features shown, see figure 3.5. For details about the stellar component of this model, see section 3.1.
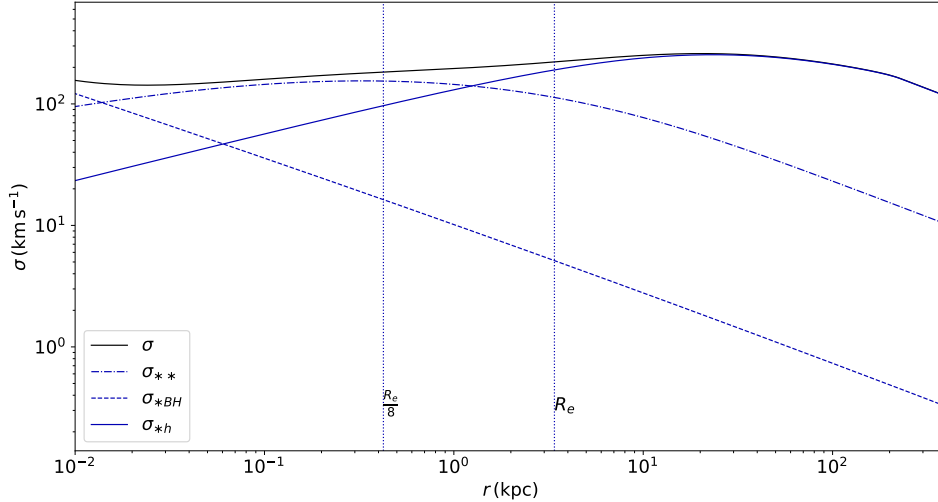
Figure 3.7: Velocity dispersion profile of the deprojected de Vaucouleurs + NFW model.
The halo is added to the de Vaucouleurs profile of figure 3.3: the total profile (black line) is the sum of the contributions of the stellar component, BH and DM halo (blue lines). For details about the stellar component, see section 3.1, while for the halo parameters see the text in this section.

dynamics at large radius, in particular, above about 10 kpc, the velocity dispersion profile matches that of the halo component. This produces a variation of the profile trend, which experiments a rise, and it decreases again at about 100 kpc; although in this very outer region, as can be seen in figure 3.1, the stellar density is very low. At $R_e/8$, the total radial profile of fig. 3.7 is higher than that of fig. 3.3; in fact, with the addition of the halo component, the projected central velocity dispersion increases and reaches the chosen value.
In the next section, we are going to show a robustness test of the code.

3.2.1 Code testing against JJ models

We test our JASMINE code against the analytical formula presented in the recent work of Ciotti and Ziaee Lorzad (2018), that give a relation between the NFW halo and the halo obtained from the so-called *JJ models*. They are spherically symmetric galaxy models in which both the stellar and total mass density distributions are described by the Jaffe (1983) profile (see eq. 2.6, in section 2.1), with clearly different scale radius and masses; the difference of mass is attributed to the DM, so a DM halo density profile is derived. The NFW profile formula, given in eq. 2.9 (section 2.2), can be written, by employing the quantities introduced by Ciotti & Ziaee Lorzad (2018), as

$$\rho_h(r) = \frac{(\mathcal{R} - 1)\rho_n}{s(\xi_h + s)^2 f(c)}; \qquad (3.2)$$

where $\mathcal{R} \equiv M_{tot}/M_*$, so $\mathcal{R} - 1 = M_h/M_*$, $\rho_n \equiv M_*/(4\pi r_*^3)$, $s \equiv r/r_*$, $\xi_h \equiv r_h/r_*$. r_* is the scale radius of the Jaffe profile, approximately related to the effective radius R_e as $r_* \simeq 4R_e/3$ (eq. 2.8); thus, we can write

$$\xi_h = \frac{r_h}{\frac{4}{3}R_e} = \frac{3}{4}\beta. \tag{3.3}$$

This is a useful substitution, because Ciotti & Ziaee Lorzad proved that the following relation between ξ_h and $\xi \equiv r_{tot}/r_*$ holds:

$$\xi_h = \sqrt{\frac{\xi}{2\,f(c)}}, \tag{3.4}$$

so that

$$\xi = \frac{9}{8}\beta^2 f(c); \tag{3.5}$$

this relation links the NFW halo with the halo analytically obtained from the JJ models. In the same paper, it was also proved an analytical expression for the stellar projected central velocity dispersion (within $R_e/8$) due to the DM halo:

$$\sigma_{*h}^2 = \frac{G\,M_*}{r_*}\frac{\mathcal{R}}{\xi}, \tag{3.6}$$

that, now, we can write

$$\sigma_{*h}^2 = \frac{G\,M_*}{r_*}\frac{8\mathcal{R}}{9\beta^2 f(c)}. \tag{3.7}$$

It means that, fixed the stellar component and the halo mass, by varying only the halo parameters, we expect that also in our numerical models $\sigma_{*h}^2 \propto \beta^{-2} f(c)^{-1}$. By fixing β and building models with only different c and then, on the contrary, by fixing c and building models with different β, we confirm that dependence of σ_{*h}. This test is a proof that the NFW halo is well numerically implemented in the JASMINE code, because it produces the results analytically derived. In the next section, a test on the models is reported.

3.3 Model testing through the dark matter fraction

In this section, we first intend to investigate the dependence of the total halo mass and its amount within the effective radius, as a function of the stellar and halo parameters. In particular, we calculate the so-called *DM fraction* ($f_{DM} \equiv M_h(R_e)/M_{tot}(R_e)$) and the DM-to-stellar mass ratio $M_h(R_e)/M_*(R_e)$, where, with these masses, we refer to the masses contained in a sphere of radius R_e (and not to the projected masses within R_e). Then, we compare our DM fractions with those inferred by dynamical models based on the observations of large samples of ETGs (from the ATLAS [3D] and SLACS surveys), in order to identify the stellar and halo parameters which produce models with *reasonable*

β	c	$\frac{M_h}{10^{12}\,M_\odot}$	$\frac{M_h}{M_*}$	$f_{DM} \equiv \frac{M_h(R_e)}{M_{tot}(R_e)}$	$\frac{M_h(R_e)}{M_*(R_e)}$
	10	10.4	127.88	0.65	1.90
7	20	14.6	179.72	0.65	1.90
	30	17.1	212.02	0.65	1.90
	10	1.02	12.62	0.61	1.56
2	20	1.44	17.75	0.61	1.56
	30	1.70	20.92	0.61	1.56

Table 3.2: Deprojected de Vaucouleurs + NFW galaxy models. The stellar component is identical and given in table 3.1. The halo component varies by varying $\beta = 2, 7$ (given in order of decreasing f_{DM}) and $c = 10, 20, 30$. For each model, the total halo mass, halo-to-stellar mass ratio, DM fraction and total halo-to-stellar mass ratio at the effective radius are given (from left to right).

dark matter fractions.

We first consider spherically symmetric galaxy models, made of a deprojected de Vaucouleurs stellar distribution embedded in a NFW halo, in order to study the role of the halo parameters β and c on the DM amount and to *test* their f_{DM}. Then, we consider models with a Jaffe stellar distribution and we study also the effect of a variation in the mass-to-light ratio $\Upsilon_{*\,dyn}$. In the previous section (3.2), instead, we commented on the impact of the halo parameters on the positions of r_h and r_t, i.e. on the shape of the NFW halo.

We build galaxy models with the same de Vaucouleurs stellar distribution and different values of β and c. The stellar component is that described in section 3.1 and shown in figures 3.1, 3.2, 3.3; its properties are reported in table 3.1. These models require a certain amount of DM to reproduce the chosen value for σ_{e8} ($= 180\,\mathrm{km\,s^{-1}}$). Here we explore models with $\beta = 2, 7$ and $c = 10, 20, 30$. These values of the concentration parameters are quite high, with respect to the cosmological predictions (e.g. Dutton and Macciò, 2014), as we will see in section 4.1.4, but our aim here is only to investigate the dependence of the DM amount and DM fraction on c, so they are illustrative of the role of c. In table 3.2, the total halo mass M_h, total halo-to-stellar mass ratio M_h/M_*, DM fraction and halo-to-stellar mass ratio at R_e are given, for six galaxy models with different β and c. First of all, we note that, by increasing β or c, M_h increases. In fact, as β or c increase, r_h and r_t move towards larger radii (as can be seen in fig. 3.5) and the influence of the halo on the inner region decreases, thus a larger M_h is required to reproduce the given σ_{e8}. Naturally, since the stellar component is fixed, the total halo-to-stellar mass ratio also increases. Nevertheless, at the effective radius, we do not see the same trend: the DM fraction and the halo-to-stellar mass ratio increase by increasing β, even if slowly, and they are constant with c. In fact, even on the total galaxy, M_h increases very slowly with c and, since this increasing halo mass is concentrated more in the outer region, because of the increasing truncation radius, it is not surprising that in the inner region the variation is not significant. Since we are interested on studying the
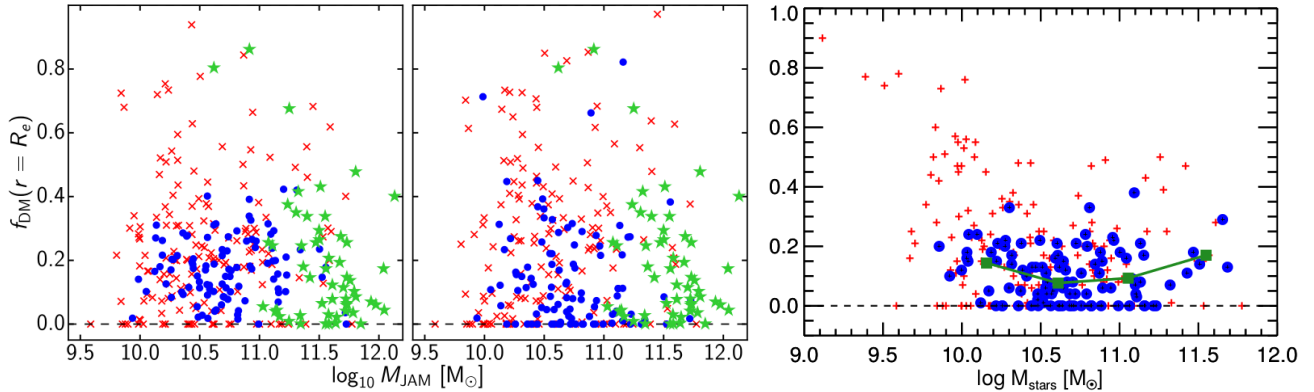
Figure 3.8: Dark matter fraction. DM fractions within R_e obtained from large galaxy samples, with different dynamical models, published in different works. In the first and second panels, the results obtained by Model I and Model II of Poci et al. (2017) for the ATLAS [3D] sample of 258 ETGs and, with green stars, the results of Posacki et al. (2015) for the SLACS sample of 55 ETGs. In the right-hand panel, the results published by Cappellari, Scott et al. (2013) from the ATLAS [3D] sample. In all figures, the blue circles represent the data with the best quality and the red crosses the data with low quality of the ATLAS [3D] sample; for details see Poci et al. (2017) and Cappellari, Scott et al. (2013), from where these figures are taken. In table 3.3, the average DM fractions are given, for each modelling.

f_{DM} (best data)	f_{DM} (full sample)	Reference
0.17	0.19	Model I, Poci et al. (2017)
0.09	0.13	Model II, Poci et al. (2017)
0.09	0.13	Cappellari, Scott et al. (2013)
-	0.14	Posacki et al. (2015)

Table 3.3: Dark matter fraction. Average DM fractions within R_e, from the samples shown in figures 3.8.

stellar dynamics in the central region of galaxies, this suggest that it is independent of the halo concentration; we will deepen this point in the next section (3.4).

Although the trend of the total DM mass, as a function of the halo parameters, respects our predictions, we find values for the DM fraction quite high, with respect to those found by dynamically modelling large samples of ETGs. We refer to the results published by Cappellari, Scott et al. (2013), Posacki et al. (2015) and Poci et al. (2017), shown in figures 3.8. Cappellari et al. and Poci et al. studied a sample of 258 ETGs from the ATLAS [3D] survey, while Posacki et al. studied a sample of 55 ETGs from the SLACS survey. As summarised in Poci et al. (2017) and reported in table 3.3, the average DM fractions computed in these works are considerably lower than the values inferred from our models. From their models, in fact, only few galaxies have a $f_{DM} \simeq 0.61 - 0.65$ and the average values are always less than 0.20, i.e. only the 20% of the matter enclosed in the sphere of radius R_e is made of dark matter, while the 80% is made of stars (and BH, remembering that the BH mass is the 0.1% of the total stellar mass). Taking into con-

Υ_{*dyn}	$\frac{M_*}{10^{10}\,M_\odot}$	c	$\frac{M_h}{10^{11}\,M_\odot}$	$\frac{M_h}{M_*}$	$f_{DM} \equiv \frac{M_h(R_e)}{M_{tot}(R_e)}$	$\frac{M_h(R_e)}{M_*(R_e)}$
		10	33.8	47.31	0.38	1.62
3.2	7.16	20	47.4	66.49	0.38	1.62
		30	56.0	78.46	0.38	1.62
		10	6.22	8.20	0.10	1.11
3.4	7.61	20	8.74	11.53	0.10	1.11
		30	10.3	13.61	0.10	1.11

Table 3.4: Jaffe + NFW galaxy models. The stellar and halo components vary by varying the mass-to-light ratio $\Upsilon_{*dyn} = 3.2, 3.4$ and $c = 10, 20, 30$, while $\beta = 7$ is fixed; for details about the stellar component, see section 3.1. Here we report, for each model, the stellar mass, total halo mass, halo-to-stellar mass ratio, DM fraction and halo-to-stellar mass ratio at the effective radius (from left to right).

sideration higher values of β would make this discrepancy worse, while we avoid values of $\beta < 2$ to keep a significant difference between the stellar and the DM distributions.

Therefore, we explore models made of a Jaffe stellar distribution embedded in a NFW DM halo. In fact, since σ_{e8} for the Jaffe profile is higher than that for the de Vaucouleurs one, the DM amount required to reproduce σ_{e8} will be lower, as mentioned in section 3.1. Thus, we expect that these models produce lower DM fractions, i.e. more in agreement with values known from the literature. Moreover, while a model with de Vaucouleurs stellar profile, $\sigma_{e8} = 180\,\mathrm{km\,s^{-1}}$ and $\Upsilon_{*dyn} = 3.62$, requires a certain DM component to reproduce σ_{e8}, an equivalent model with Jaffe stellar profile will overestimate σ_{e8}. This means that, fixed σ_{e8}, a model with Jaffe stellar profile requires a certain DM component only with a lower Υ_{*dyn}, i.e. a lower M_*. We will discuss about it in section 4.1; for now, we consider two different values of Υ_{*dyn}, both in agreement with values obtained in section 4.1, meaning both requiring a certain DM component, in order to see the dependence of f_{DM} on the mass-to-light ratio and to find *reasonable* f_{DM} values. These mass-to-light ratios are $\Upsilon_{*dyn} = 3.2, 3.4$. We fixed $\sigma_{e8} = 180\,\mathrm{km\,s^{-1}}$ as example; of course, models characterised by a higher σ_{e8} would require more M_h. Since the dependence of f_{DM} on β is not strong, we fix $\beta = 7$ for these models, while $c = 10, 20, 30$, as before. In table 3.4, in analogy with table 3.2 for the de Vaucouleurs + NFW galaxy models, we give the total halo mass, total halo-to-stellar mass ratio, DM fraction and halo-to-stellar mass ratio at the effective radius, for six Jaffe + NFW galaxy models, with different Υ_{*dyn} and c. As observed for the de Vaucouleurs + NFW models, by increasing c, the total halo mass (and also the total halo-to-stellar mass ratio) required to reproduce the given σ_{e8} increases, while the DM fraction and the halo-to-stellar mass ratio at the effective radius remain constant. Moreover, as expected, by increasing the mass-to-light ratio, the halo mass decreases and also the fractions at the effective radius decrease. Contrary to the dependence on β previously discussed, f_{DM} varies significantly by varying Υ_{*dyn}. In fact, we see that for $\Upsilon_{*dyn} \simeq 3.4$, our galaxy models produce f_{DM} values in agreement with those found by Cappellari, Scott et al.

(2013), Posacki et al. (2015) and Poci et al. (2017). While for much higher $\Upsilon_{*\,dyn}$, no DM fraction would be necessary, and for much lower $\Upsilon_{*\,dyn}$, a DM fraction too high would be required. It means that we can build Jaffe + NFW galaxy models with a dark matter fraction consistent with those derived from dynamical models based on large samples of observed ETGs, by assuming an appropriate value for $\Upsilon_{*\,dyn}$. Furthermore, also with de Vaucouleurs + NFW models, we can obtain reasonable values for f_{DM}, on the condition of assuming higher $\Upsilon_{*\,dyn}$, but not so high that the DM is no longer required. Therefore, for both de Vaucouleurs and Jaffe + NFW models, we could calculate a *range* for the mass-to-light ratio, from a *minimum* value, corresponding to a maximum f_{DM} that we decide to accept, according to the other dynamical models seen, up to a *maximum* value, corresponding to the limit model in which stars and BH alone reproduce the given σ_{e8}, without the addition of any DM. In the next chapter 4, section 4.1, instead, we are going to calculate a range for the mass-to-light ratio in order to be in accordance with values derived from Simple Stellar Population (SSP) synthesis models. In future, we could consider both other dynamical models and SSP synthesis models, in order to find more tighter and robust constraints on the mass-to-light ratio.

3.4 Effect of the truncation radius on the velocity dispersion

In the previous section, we noted that the halo-to-total and halo-to-stellar mass ratios at the effective radius ($f_{DM} \equiv M_h(R_e)/M_{tot}(R_e)$ and $M_h(R_e)/M_*(R_e)$ respectively) are constant with c, that means they are not affected by a variation of the truncation radius r_t of the NFW DM halo. This suggest that, at radius small enough, also the stellar dynamics could be not affected by a variation of r_t. Since we are interested, in particular, to the projected velocity dispersion at $R_e/8$, we verify that, fixed the stellar component, β and M_h, it does not change by varying the halo concentration, i.e. the solution of the vertical JE (see appendix A and B), in a region central enough, is independent on the halo concentration.

This is not surprising, for two main reasons. First, the contribution to the velocity dispersion due to the DM component is

$$\rho_* \sigma_{*h}^2 = \int_z^\infty \rho_* \frac{\partial \phi_h}{\partial z'} dz', \tag{3.8}$$

where

$$\frac{\partial \phi_h(r)}{\partial z} = \frac{GM_h(r)}{r^3} z. \tag{3.9}$$

If the halo is truncated at a certain radius r_t, then $M_h(r \geq r_t) = M_h = const$, so

$$\left. \frac{\partial \phi_h(r)}{\partial z} \right|_{r \geq r_t} \propto \frac{z}{r^3}; \tag{3.10}$$

if, instead, the halo is not truncated, $M_h(r \geq r_t) \propto \ln r$, so it increases slowly with r and

$$\left. \frac{\partial \phi_h(r)}{\partial z} \right|_{r \geq r_t} \propto \frac{z \ln r}{r^3}. \tag{3.11}$$

Therefore, if the halo is or is not truncated, the force (per unit mass) that it produces along the z-axis have only a slight difference at the boundary conditions and it does not affect significantly the central velocity dispersion. Furthermore, and this is the second reason, at such a large radius, the stellar density entering in the integral of eq.3.8 is very low, thus the contribution to the total velocity dispersion, due to the DM distributed above r_t, is very low.

This allows us to fix an arbitrary value of r_t, e.g. $r_t = 10\,r_h$, or even not to truncate the NFW halo, and solve the JEs without fixing a value for c. Until now, by solving the vertical JE equation, fixed the stellar properties and the halo parameters β and c, we have found the halo mass M_h required to reproduce the given σ_{e8}. Now, instead, we can multiply the NFW density, potential and forces (see section 2.2) by the function $f(c)$ and find the required value for $M_h/f(c)$, in a way detailed in section 4.1.1. This allows, for chosen values of σ_{e8}, $\Upsilon_{*\,dyn}$ and β, to identify not only one model with the necessary M_h, but a *family* of models characterised by the same ratio $M_h/f(c)$ and different values of M_h and c. In the next section, we show a tool to vary both the stellar and dark distribution, building more realistic models, in order to explore how much the total mass of the dark matter halo can vary, while reproducing the projected central velocity dispersion of stars.

Chapter 4

Main results

In this chapter, we investigate the influence of the dark matter distribution on the projected velocity dispersion profile of stars. In particular, we attempt to understand how much observations of the velocity dispersion in the central region of ETGs are able to give constraints on the DM amount and distribution. In the first section (4.1), we explore the mass and concentration that a NFW halo profile can have, reproducing the observed central kinematic features of galaxies. In the second section (4.2), we investigate the possibility of a different DM distribution and the total mass which can be distributed in the outer region of galaxies, still reproducing the kinematic field observed in their inner region.

4.1 Constraints on the halo mass from observations within $R_e/8$ and SSP synthesis models

The first question is how much the structure of the dark matter halo can vary, reproducing the projected velocity dispersion profile of stars. In particular, we fix a NFW DM profile, with scale radius given by $r_h = \beta R_e$, where $\beta = 7$, and truncation radius $r_t = 10 r_h$. We showed, in fact, in section 3.4, that the stellar projected velocity dispersion in the inner region of galaxies is not affected by a variation of the truncation radius position, located in the outer region; thus, we fix now an arbitrary value for r_t and we do not fix the concentration c in the NFW profile formula (section 2.2). In this way, we shall be able to find a variety of value pairs (c, M_h) permitted by the observation of the projected velocity dispersion, measured within a certain radius, as schematically illustrated in diagram of fig. 4.1.

In the present thesis work, we confine our study to spherical and isotropic galaxy models and to observations within $R_e/8$. So the flattening parameter is $q = 1$, there is no rotation ($\overline{v_R} = \overline{v_z} = \overline{v_\varphi} = 0$) and $\sigma_R = \sigma_z = \sigma_\varphi \equiv \sigma$; the anisotropy parameter of Satoh is fixed $k = 1$ (see appendix B). We reserve for the future the extension of this study to the more general case of axisymmetric (oblate) models, with a given degree of flattening

$(0.3 \leq q < 1)$ and a given anisotropy of the velocity dispersion tensor $(0 \leq k < 1)$, so $\sigma \equiv \sigma_R = \sigma_z \neq \sigma_\varphi$. We therefore identify a region in the $c - M_h$ plane where halos reproduce σ_{e8}, that means observations of the stellar velocity dispersion within the radius $R_e/8$ are consistent with a range of halo masses, associated to a range of concentrations.

4.1.1 Dependence on the mass-to-light ratio

From the vertical Jeans equation, the velocity dispersion σ^2 is calculated and can be written as the sum of the contributions of all the matter components of the galaxy (stars, BH, DM), thanks to the linearity of the JEs. This is obviously true at any radius, thus:

$$\sigma_{e8}^2 = \sigma_{**}^2 + \sigma_{*BH}^2 + \sigma_{*h}^2, \tag{4.1}$$

where σ_{**}^2, σ_{*BH}^2, σ_{*h}^2 are the components of the squared central velocity dispersion due to the contributions of the gravitational potentials of the stars themselves, BH and halo, respectively. Hereafter, we imply these velocity dispersions are values calculated as luminosity-weighted within a radius of $R_e/8$, albeit we omit it in formula. Since any potential is linearly proportional to the total mass of the associated distribution, and moreover $M_{BH} = 10^{-3} M_*$ (see chapter 2), then also σ_{*BH}^2 depends on the stellar mass, we can define the following helpful quantities:

$$\tilde{\sigma}_*^2 \equiv \tilde{\sigma}_{**}^2 + \tilde{\sigma}_{*BH}^2 \equiv \frac{\sigma_{**}^2 + \sigma_{*BH}^2}{M_{*10}} \quad (\mathrm{km^2\,s^{-2}}) \tag{4.2}$$

and

$$\tilde{\sigma}_{*h}^2 \equiv \sigma_{*h}^2 \frac{f(c)}{M_{h10}} \quad (\mathrm{km^2\,s^{-2}}), \tag{4.3}$$

where

$$M_{*10} \equiv \frac{M_*}{10\,M_\odot}, \quad M_{h10} \equiv \frac{M_h}{10^{10}\,M_\odot} \tag{4.4}$$

and $f(c)$ is the function of the concentration entering the NFW formula, as defined in section 2.2 and shown in section 3.2. $\tilde{\sigma}_*^2$ and $\tilde{\sigma}_{*h}^2$ are thus constant for all models with the same σ_{e8} and β, i.e. for each *family* of models. Thus eq. 4.1 can be written in the equivalent form

$$\sigma_{e8}^2 = M_{*10}\, \tilde{\sigma}_*^2 + \frac{M_{h10}}{f(c)}\, \tilde{\sigma}_{*h}^2, \tag{4.5}$$

where we introduce $\alpha \equiv M_{h10}/f(c)$.

In this way, the only quantities depending on the model are M_*, M_h and c. The normalisations of the two contributions are both in units of $10^{10}\,M_\odot$ and can be easily compared; furthermore, we divide the halo mass by the function of c, in order to obtain value pairs (c, M_h). We can now obtain a family of models reproducing a given σ_{e8}, by increasing the stellar mass and coherently decreasing the halo mass or viceversa. The diagram of figure 4.1 summarises the logical tool.

We can identify two limit cases: (1) a model without DM ($M_{h10} = 0$), with the maximum stellar mass, which we define M_{*10}^0; (2) a model with the maximum amount of
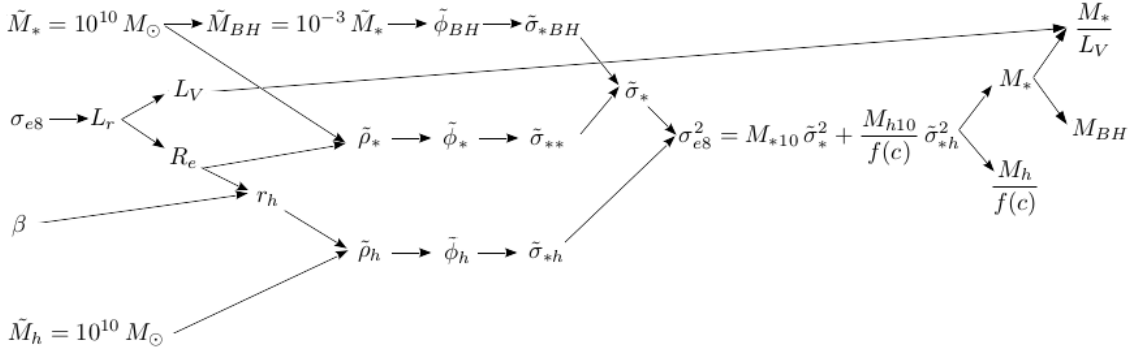
Figure 4.1: Diagram without fixing the mass-to-light ratio. The projected central velocity dispersion σ_{e8} and the halo-to-stellar scale radius β are fixed, determining a *family* of models, and the stellar mass and halo mass are fixed to $10^{10} M_\odot$. Then, σ_{e8} provides the effective radius R_e and the luminosity L_V, through the SLs. The halo scale radius r_h and the density, gravitational potential and velocity dispersion due to each component (stars, BH, DM) are consequently calculated. Finally the total projected velocity dispersion computed within $R_e/8$ is compared to the given σ_{e8} and value pairs $M_* - M_h/f(c)$ are calculated to reproduce it. The BH mass, M_{BH}, only depends on the stellar mass. The mass-to-light ratio is the ratio between the computed stellar mass and the luminosity derived from the SLs, that we call in the text $\Upsilon_{*\,dyn}$.

DM (M_{h10}^{max}) and the minimum stellar mass, M_{*10}^{min}. The first model is simply obtained by fixing $M_{h10} = 0$ in eq. 4.5. For the second model, we have to establish a criterion to define the minimum value for the stellar mass. For this purpose, we consider that all models with the same σ_{e8} (i.e. of the same family) have the same luminosity in each band (e.g. L_V), so a variation in the stellar mass corresponds to a variation in the stellar mass-to-light ratio, for example, in the V band, that we define $\Upsilon_{*\,dyn} \equiv M_*/L_V$. Thus, we choose for reference the mass-to-light ratios obtained by Evolutionary Population Synthesis models (EPS). For simplicity, we consider that stars formed in a single burst, so there is a single population, characterised by the same age and metallicity. This analysis requires Simple Stellar Population synthesis models (SSP), for which we refer to Maraston (2005), by considering mass-to-light ratios associated to age and metallicity appropriate for our models, as described in the next section 4.1.2.

The relation 4.5 can be easily expressed as a function of $\Upsilon_{*\,dyn}$, instead of M_{*10}. We first note that, in case of no DM, 4.5 gives a trivial expression for σ_{e8}:

$$\sigma_{e8}^2 = M_{*10}^0 \, \tilde{\sigma}_*^2, \tag{4.6}$$

thus we can write

$$M_{*10}^0 \, \tilde{\sigma}_*^2 = M_{*10} \, \tilde{\sigma}_*^2 + \frac{M_{h10}}{f(c)} \, \tilde{\sigma}_{*h}^2. \tag{4.7}$$

By dividing both sides of this equation by $\tilde{\sigma}_*^2 \, L_V \, 10^{-10}$, it becomes

$$\frac{M_*^0}{L_V} = \frac{M_*}{L_V} \left(1 + \frac{M_h}{M_* f(c)} \frac{\tilde{\sigma}_{*h}^2}{\tilde{\sigma}_*^2} \right), \tag{4.8}$$

so

$$\Upsilon^0_{*dyn} = \Upsilon_{*dyn} \left(1 + \frac{M_h}{M_* f(c)} \frac{\tilde{\sigma}^2_{*h}}{\tilde{\sigma}^2_*} \right)$$

$$\frac{\Upsilon^0_{*dyn}}{\Upsilon_{*dyn}} = 1 + \frac{M_h}{M_* f(c)} \frac{\tilde{\sigma}^2_{*h}}{\tilde{\sigma}^2_*}, \tag{4.9}$$

where Υ^0_{*dyn} is defined as the mass-to-light ratio required to reproduce a given σ_{e8} in absence of DM.

It is clear now that, for each family, the coherent variation of M_*, M_h and c is only given by the variation between Υ_{*dyn} and Υ^0_{*dyn}, that represents how much the mass-to-light ratio can decrease from the maximum value. In practice, we are interested in finding a *range* of possible α values corresponding to a *range* of Υ_{*dyn} values, where we defined $\alpha \equiv M_{h10}/f(c)$. Since mass-to-light ratio values deriving from synthesis models are error-free, we consider for Υ_{*dyn} the possibility to vary due to uncertainties on age and metallicity, as shown by observations from the ATLAS [3D] survey (McDermid et al., 2015), as explained in section 4.1.2. Then the minimum value (Υ^{min}_{*pop}) corresponds to the minimum age and metallicity estimated for galaxies within a certain σ_{e8}, while the maximum value (Υ^{max}_{*pop}) corresponds to the maximum estimated age and metallicity. This defines a range $[\Upsilon^{min}_{*pop}, \Upsilon^{max}_{*pop}]$ in which Υ_{*dyn} can vary. For each family of models, we can find values of Υ^0_{*dyn} below, inside or above that range, identifying three different situations.

(1) If $\Upsilon^{min}_{*pop} < \Upsilon^0_{*dyn} < \Upsilon^{max}_{*pop}$, it is possible to add a DM halo and decrease Υ_{*dyn} down to the lower limit; that limit corresponds to the maximum DM amount which can be present in such a model, reproducing the projected central velocity dispersion and with a stellar mass-to-light ratio in agreement with results of SSP synthesis models. On the other hand, obviously, it is never possible to increase Υ_{*dyn} above Υ^0_{*dyn}, because the latter is the mass-to-light ratio in absence of DM, so a larger value, i.e. a larger stellar mass, would not reproduce σ_{e8}. It means that, for models characterised by this σ_{e8} value, stars and BH can reproduce the central stellar velocity dispersion, without the addition of any DM fraction and in agreement with results of SSP synthesis models. The range for Υ_{*dyn} in this case become

$$\Upsilon^{min}_{*pop} < \Upsilon_{*dyn} < \Upsilon^0_{*dyn}, \tag{4.10}$$

which provides the following range for $\alpha \equiv M_{h10}/f(c)$:

$$0 < \alpha < \alpha^{max}, \tag{4.11}$$

where the *maximum* halo is associated to the *minimum* stellar component; while, the *maximum* stellar component corresponds to M^0_{*10} (i.e. $\alpha = 0$), so $M^{max}_{*10} = M^0_{*10}$. Thus, in the $c - M_h$ plane it is defined an *half-plane*, limited by

$$\alpha^{max} = \left. \frac{M_{h10}}{f(c)} \right|_{max} = \frac{M^{max}_{h10}}{f(c)}. \tag{4.12}$$
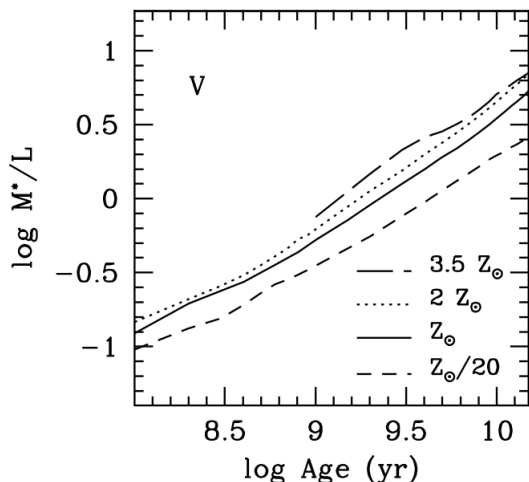
Figure 4.2: Mass-to-light ratio. Dependence of the mass-to-light ratio in the V band (in solar units), on age (yr) and metallicity ($Z_\odot$), from SSP synthesis models of Maraston (2005), adopting a Kroupa IMF. The figure is taken from Maraston (2005). In our thesis work, in agreement with other works (e.g. Cappellari et al., 2012; Cappellari, 2016), we call the mass-to-light ratio deriving from SSP synthesis models Υ_{*pop}.

(2) If $\Upsilon^0_{*dyn} > \Upsilon^{max}_{*pop}$, the models necessarily requires a DM fraction, in order to have Υ_{*dyn} inside the range expected for the stellar population, thus:

$$\Upsilon^{min}_{*pop} < \Upsilon_{*dyn} < \Upsilon^{max}_{*pop} \tag{4.13}$$

and

$$\alpha^{min} < \alpha < \alpha^{max}, \tag{4.14}$$

where the *maximum* stellar component corresponds to the *minimum* halo. Now, in the $c - M_h$ plane a *band* is defined, limited by α^{min} and α^{max}.

(3) Finally, if $\Upsilon^0_{*dyn} < \Upsilon^{min}_{*dyn}$, it means that even stars and BH alone produce a projected central velocity dispersion grater than given σ_{e8} value. Thus, it is not possible to build models, through this tool, with this σ_{e8} value: these models have to be rejected.

In the next section, we are going to illustrate the technique with which the ranges of mass-to-light ratios are derived, for three families of models with $\sigma_{e8} = 180, 210, 250 \, \mathrm{km\,s^{-1}}$, taken as example.

4.1.2 Range for the mass-to-light ratio

As explained in the previous section, for a given σ_{e8}, we intend to find a range for the mass-to-light ratio Υ_{*dyn}, in order to define a range of $\alpha \equiv M_{h10}/f(c)$ values, which include all halos reproducing the projected central velocity dispersion σ_{e8}. We derive the mass-to-light ratio (Υ_{*pop}) as a function of the age and metallicity of the population, with reference to the SSP synthesis models of Maraston (2005) (figure 4.2). These mass-to-light ratios are computed with an algorithm based on the *fuel consumption theorem*, by taking the stellar mass losses into account and with the relation between living stars and remnants (white dwarfs, neutron stars, black holes) as given in Renzini and Ciotti (1993). Moreover, we refer to models in which a Kroupa IMF (Kroupa, 2001) is adopted, instead of the original Salpeter IMF (Salpeter, 1955), because a "lighter" slope at the lower masses seems to describe better the population formation in ETGs.

Since Υ_{*pop} is error-free, the range of mass-to-light ratios is obtained by considering the uncertainties on the measures of age and metallicity within radius $R_e/8$, as reported in McDermid et al. (2015). This paper is part of *The ATLAS* ^{3D} *Project*, which analyses 258 ETGs from the ATLAS ^{3D} survey. They report the age t_{Gyr} and metallicity $[Z/H]$ as a function of $\log(\sigma_e)$, for the aperture radius $R_e/8$ (and also $R_e/2$, R_e); they fit data with a linear fit, providing the standard deviation σ (figure 4.3). We show also their results from observations at aperture radius $R_e/2$, R_e, even if we do not use them now, but which would allow to extend the present work to larger apertures. The standard deviation on
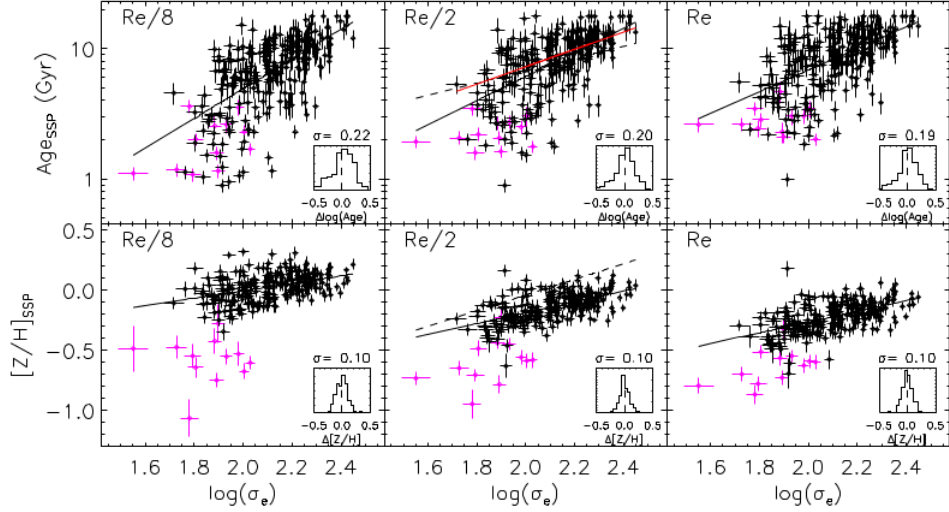

Figure 4.3: Age and metallicity. As a function of $\log(\sigma_e)$, for the aperture radius $R_e/8$, $R_e/2$, R_e, from the ATLAS ^{3D} survey. The figure is taken from McDermid et al. (2015). In the text, we call the age t_{Gyr} and the metallicity $[Z/H]$.

the measures at $R_e/8$ are $\sigma = 0.22$ on $\log(t_{Gyr})$ and $\sigma = 0.10$ on $[Z/H]$. From data shown in figure 4.3, we identify a range in age and metallicity for a certain projected velocity dispersion within the effective radius (σ_e). Then, for those ranges, using the SSP synthesis models of Maraston (2005), we derive the range of mass-to-light ratio in the V band; we refer, in particular, to her work of 2005 (see figure 4.2) and to the more complete tabulated values (*http://www.icg.port.ac.uk/ maraston/SSPn/ml/ml_SSP.tab*).

For all studied model families ($\sigma_{e8} = 180$, 210, 250 $\mathrm{km\,s^{-1}}$), we find that stars and BH can reproduce the projected central velocity dispersion even without the addition of a DM component, i.e. we find the case $\Upsilon_{*pop}^{min} < \Upsilon_{*dyn}^0 < \Upsilon_{*pop}^{max}$, so the mass-to-light ratio range for these models is $\Upsilon_{*pop}^{min} < \Upsilon_{*dyn} < \Upsilon_{*dyn}^0$, as in case (1) illustrated in the previous section. Then, we only need to calculate Υ_{*pop}^{min}, corresponding to the lower limits on age and metallicity. These results are shown in table 4.1. As known from the study of galaxies (and as fig. 4.3 shows), more massive galaxies are in general older and more metal-rich than less massive ones. In fact, also the minimum values of age and metallicity increase by increasing σ_{e8}, so the range of Υ_{*dyn} moves towards higher values. For all our models, the metallicity is near to the solar metallicity ($[Z/H] = 0$).

σ_{e8}	R_e	L_V	t^{min}	$[Z/H]^{min}$	$[\Upsilon_{*pop}^{min}, \Upsilon_{*dyn}^0]$
$(\mathrm{km\,s^{-1}})$	(kpc)	$(10^{10}\,\mathrm{L_\odot})$	(Gyr)		$(\mathrm{M_\odot\,L_\odot^{-1}})$
180	3.26	2.23	4.5	-0.07	[1.63,3.45]
210	4.57	3.97	5.0	-0.05	[1.86,3.70]
250	7.04	7.83	6.0	-0.02	[1.93,4.10]

Table 4.1: Range for the mass-to-light ratio. For each studied family of models (σ_{e8} = 180, 210, 250 km s^{-1}), the effective radius R_e and the V band-luminosity are computed from the SLs. t^{min} and $[Z/H]^{min}$ are the minimum value of age and metallicity, respectively, derived from observations of McDermid et al. (2015). Υ_*^{min} is the associated mass-to-light ratio in the V band, derived from SSP synthesis models of Maraston (2005); Υ_{*dyn}^0 is instead the mass-to-light ratio derived for a model without DM.

We preliminarily conclude that observations of the stellar velocity dispersion within a radius of $R_e/8$ can not determine whether DM is present or not and, if present, its total amount. We do not claim to prove that ETGs could not contain any DM fraction, because in last years different fields of Astrophysics have provided evidences of the existence of DM halos surrounding galaxies. To name a few of the studies which permit to measure the total mass of galaxies: the spiral galaxy rotation curve, the gravitational lensing, the temperature of hot X-gas corona (in hydrostatic equilibrium), the velocity dispersion of stars in galaxies and that of galaxies in clusters (satisfying the Virial Theorem). Our aim is instead to investigate how much the DM halo mass can vary, with a coherent variation of the stellar mass, still reproducing kinematic observations in their central region. In the next sections, we are going to present our results.

4.1.3 Results on the stellar and halo masses and $c - M_h$ plane

After the discussion of the previous sections, we are now able to calculate a stellar mass M_* and a halo mass M_h for each Υ_{*dyn} value inside the range calculated, so we can see how much models with the same σ_{e8} and β can contain different contributions of stars (and BH) and DM. The minimum stellar mass is simply obtained from the definition of the mass-to-light ratio (see eq. 4.8):

$$M_{*10}^{min} = \Upsilon_{*pop}^{min} L_V 10^{-10}, \tag{4.15}$$

while, for the associated maximum halo mass, we calculate α^{max} from eq. 4.7:

$$\alpha^{max} \equiv \frac{M_{h10}^{max}}{f(c)} = \left(M_{*10}^{max} - M_{*10}^{min} \right) \frac{\tilde{\sigma}_*^2}{\tilde{\sigma}_{*h}^2} =$$
$$= \left(\Upsilon_{*dyn}^0 - \Upsilon_{*pop}^{min} \right) L_V 10^{-10} \frac{\tilde{\sigma}_*^2}{\tilde{\sigma}_{*h}^2}, \tag{4.16}$$

where $\tilde{\sigma}_*^2$ and $\tilde{\sigma}_{*h}^2$ are computed from the definitions in equations 4.2 and 4.3, respectively. As previously discussed, the opposite limit case is given by M_{*10}^{max} and $\alpha = 0$ (i.e. $M_{h10} =$

σ_{e8} (km s^{-1})	$\tilde{\sigma}_* \equiv \sigma_*/\sqrt{M_{*10}}$ (km s^{-1})	$\tilde{\sigma}_{*h} \equiv \sigma_{*h}/\sqrt{M_{h10}/f(c)}$ (km s^{-1})	$[M_{*10}^{min}, M_{*10}^{max}]$	$\alpha^{max} \equiv M_{h10}^{max}/f(c)$
180	64.83	3.19	[3.65,7.70]	1672.73
210	54.75	2.69	[7.38,14.69]	3028.18
250	44.12	2.17	[15.11,32.10]	7023.36

Table 4.2: Stellar and halo masses. For each family of models, characterised by a given σ_{e8}, related values of $\tilde{\sigma}_*^2$ and $\tilde{\sigma}_{*h}^2$ are computed; $[M_{*10}^{min}, M_{*10}^{max}]$ is the range of values for the stellar mass, in agreement with the range of mass-to-light ratios, derived from SSP synthesis models and reported in table 4.1; $[0, \alpha^{max}]$ is the range of values for the halo mass. M_{*10}^{max} is associated to $\alpha = 0$ and M_{*10}^{min} is associated to α^{max}.

0). In table 4.2, these values are reported for any model family. Figure 4.4 shows the linear relation

$$\alpha = \left(\Upsilon_{*\,dyn}^0 - \Upsilon_{*\,dyn}\right) L_V \, 10^{-10} \, \frac{\tilde{\sigma}_*^2}{\tilde{\sigma}_{*h}^2}, \tag{4.17}$$

equivalent to eq. 4.7, between α and $\Upsilon_{*\,dyn}$ in all the range of $\Upsilon_{*\,dyn}$, for $\sigma_{e8} = 180$, 210, $250\,\mathrm{km\,s^{-1}}$. The minimum and maximum values of $\Upsilon_{*\,dyn}$ depend on the uncertainties on age and metallicity considered for each σ_{e8}; the range of $\Upsilon_{*\,dyn}$ is then somewhat dependent on the observations considered; furthermore, we do not consider any uncertainty on the measure of the velocity dispersion. In order to deepen our study, we could evaluate the opportunity of a different computation of the range for the mass-to-light ratio; in this way we could also determine how much it would affect our present results.

We can conclude that, through the investigation we presented, observations of the projected velocity dispersion within $R_e/8$, by considering uncertainties on the age and metallicity measures at $R_e/8$, allow a wide possibility in the halo structure. In fact, we find that the stellar mass-to-light ratio, and so the stellar mass, varies of about a factor of 2. While α varies from 0 up to about $10^{13} - 10^{14}\,M_\odot$, i.e. up to about values two orders of magnitude larger than the associated stellar mass.

We remember that α represents the halo mass divided by a function of the concentration parameter c, therefore after calculating α^{max}, we are now able to identify a region in the $c - M_h$ plane, populated by all halos permitted by the observation of a certain projected central velocity dispersion. It means that, for each σ_{e8}, all halos with value pairs (c, M_h) below the curve given by $\alpha^{max} = M_{h10}^{max}/f(c)$ reproduce the given σ_{e8}; indeed, α^{max} represents the maximum halo mass available by varying the halo concentration. On the other side, the region above this curve is populated by halos which produce a projected central velocity dispersion of stars too high, no more reproducing the given σ_{e8}. We show this situation on the $c - M_h$ plane, for our model families, in fig. 4.5. Therefore, observations of the velocity dispersion in such a central region $(R_e/8)$ allow a wide variety of halos with different values of mass and concentration. Note that α depends on c through the function

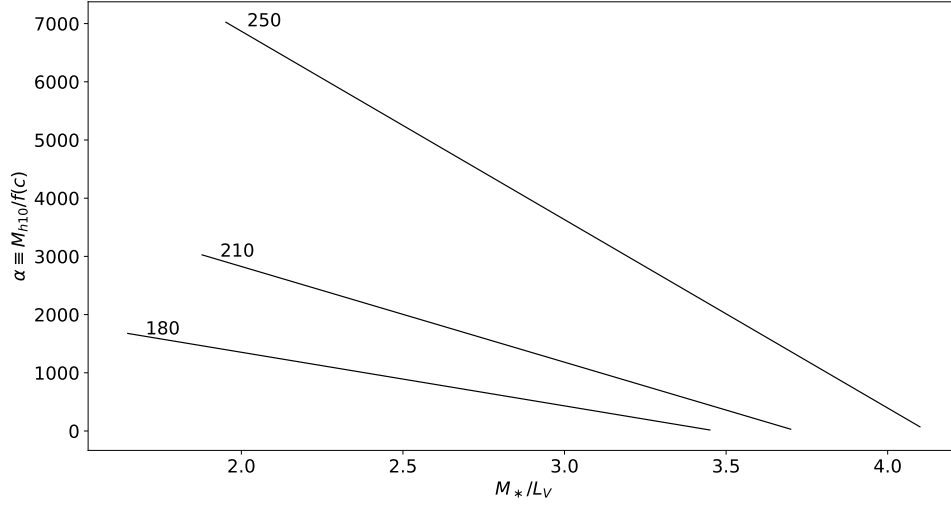$$f(c) = \ln(1 + c) - \frac{c}{1 + c}, \tag{4.18}$$

Figure 4.4: Dependence of α on the mass-to-light ratio. Relation 4.17 for models with $\sigma_{e8} = 180$, 210, 250 km s^{-1}, shown in the range $[\Upsilon_{*pop}^{min}, \Upsilon_{*dyn}^0]$ related to each σ_{e8}. The maximum value of α for each σ_{e8} (α^{max}) is provided in table 4.2.
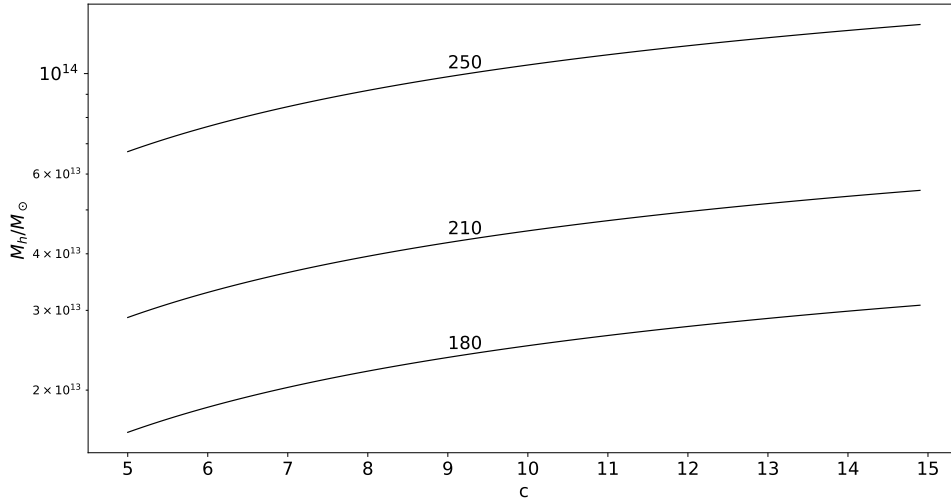

Figure 4.5: $c - M_h$ plane. The curves represent $\alpha^{max} = M_{h10}^{max}/f(c)$, for each model family characterised by a given $\sigma_{e8} = 180$, 210, 250 km s^{-1}. All the DM halos below this curve are permitted by the corresponding value of the projected central velocity dispersion of stars σ_{e8}.
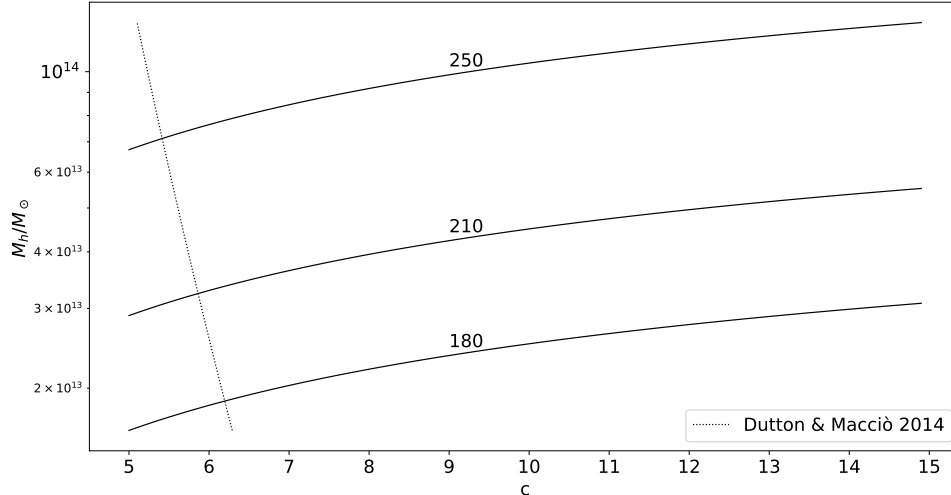
Figure 4.6: $c - M_h$ relation. Comparison between our results shown in fig. 4.5 with the *concentration-mass relation* taken from Dutton and Macciò (2014), derived for NFW DM halos, in the Cosmology from the *Planck* satellite.

shown in figure 3.4 (section 3.2), which increases slowly by increasing c: for c in the range $[5, 15]$, its value varies from about 1 up to about 2, in fact, M_h increases slowly with c, fixed α. This also suggest that we do not go far wrong on the computation of the halo mass if we fix the concentration to an arbitrary value, as we do in tests of chapter 3 and in the next section 4.2.

4.1.4 Comparison with cosmological simulations

Until now, we have not imposed any constraints on the value of c. Nevertheless, we know that cosmological N-body numerical simulations predict a relation between the halo mass and its concentration ($c \propto M_h^{\sim -0.1}$). Our aim is not to discuss here about these predictions; we decided to ignore this relation, because we want to explore the possibility to vary the DM halo, only by reproducing observable properties of ETGs. In this section, we only show the opportunity to compare our results with cosmological predictions. We refer to the *concentration-mass relation* found by Dutton and Macciò (2014), derived for NFW DM halos, in the Cosmology from the *Planck* satellite:

$$\log c = 0.905 - 0.101 \log\left(\frac{M_h}{10^{12} \, h^{-1} \, M_\odot}\right). \tag{4.19}$$

We report our fig. 4.5, with the addition of this relation in fig. 4.6. Therefore, for each σ_{e8}, we can identify, from the wide variety of value pairs ($c - M_h$) that we have found (see the previous section), those in agreement with cosmological predictions. In other words, value pairs below the curve of α^{max} and lying on the dotted curve represent halos

reproducing the projected central velocity dispersion and also satisfying cosmological predictions.

4.2 Addition of an external dark matter distribution

In the previous section, we explored the impact of a NFW dark matter halo on the projected central velocity dispersion of stars; now, instead, we investigate the impact of a different DM distribution. The NFW profile was found by Navarro, Frenk and White (Navarro et al., 1996) from cosmological N-body simulations, while we intend to investigate how much a different distribution would affect observable kinematic properties of galaxies, in particular we refer to the velocity dispersion profile of stars. We do not attempt to find a better density profile for the dark matter component, but to show that other possibilities could be still consistent with observations, at least if the distribution diverges from the NFW one only at radius outer *enough* from the aperture radius taken into consideration. In other words, we ask if a different density profile would produce a remarkably different velocity dispersion profile and how much mass should be contained to produce observable variations. We consider a quite simple additional distribution, modelled by a thin gaussian function with the centre at a radius r_0, chosen in the region where the NFW profile decreases as r^{-3}, which means between r_h and r_t. This *external* (ext) isotropic distribution is described in section 2.2.

We explore the impact of this additional gravitational contribution on a model with a given σ_{e8}, by fixing the stellar and halo components, in a way that σ_{e8} is reproduced. In practice, we fix $\sigma_{e8} = 180\,\mathrm{km\,s^{-1}}$ and the mass-to-light ratio $\Upsilon_{*dyn} \equiv M_*/L_V$ is given to be consistent with values from Maraston (2005) for this σ_{e8} (as described in section 2.3 and shown in fig. 4.1). The V-band luminosity and the effective radius are derived from the SLs and the total stellar mass is consequently computed, modelled by a deprojected de Vaucouleurs density profile. The NFW halo mass is, instead, computed to reproduce σ_{e8}, by fixing $\beta = 7$ and $c = 10$. The position of the peak and the extension of the external DM profile are fixed as a function of the halo parameters: $r_0 = r_t/2$, where $r_t = 10\,r_h$; while, the extension is represented by the standard deviation of the gaussian distribution and it is fixed as $b = r_h$. The total DM density profile is the sum of the NFW and external ones.

In table 4.3 we report the main properties of models studied in this section. They are built with the same stellar and halo components and the same parameters r_0 and b of the external distribution, which define its shape. While the external mass M_{ext}, i.e. the normalisation of the profile, varies from 0 (DM component only due to the NFW one) to values which are comparable to M_h, and so comparable to the total mass of each model. In figures 4.7 and 4.8, the density profiles of these models are compared. As can be seen, for each model, the external density profile is negligible with respect to the NFW one, up to a radius near to r_0, where they become more or less comparable, according to the M_{ext} value. In fact, for M_{ext} up to two orders of magnitude lower than M_h, the total density profile is not affected by the additional component, at radius where the halo is present; for $M_{ext} \gtrsim M_h$, instead, the total density increases remarkably at large

σ_{e8} $(\mathrm{km\,s^{-1}})$	Υ_{*dyn}	R_e (kpc)	L_{V10}	M_{*10}	β	c	M_{h10}	M_{ext10}
								0
								10
180	3.62	3.26	2.23	8.10	7	10	$1.04\cdot10^3$	10^2
								10^3
								10^5

Table 4.3: Models with external DM distribution. Five dynamical models, with the same stellar and halo components, and different contributions of the external DM component. The first model has no external component, to show the impact, on the projected velocity dispersion profile, of the addition of more and more dark matter. Here $L_{V10} \equiv L_V/(10^{10}\,L_\odot)$ and $M_{ext10} \equiv M_{ext}/(10^{10}\,M_\odot)$, while other quantities have been previously defined.
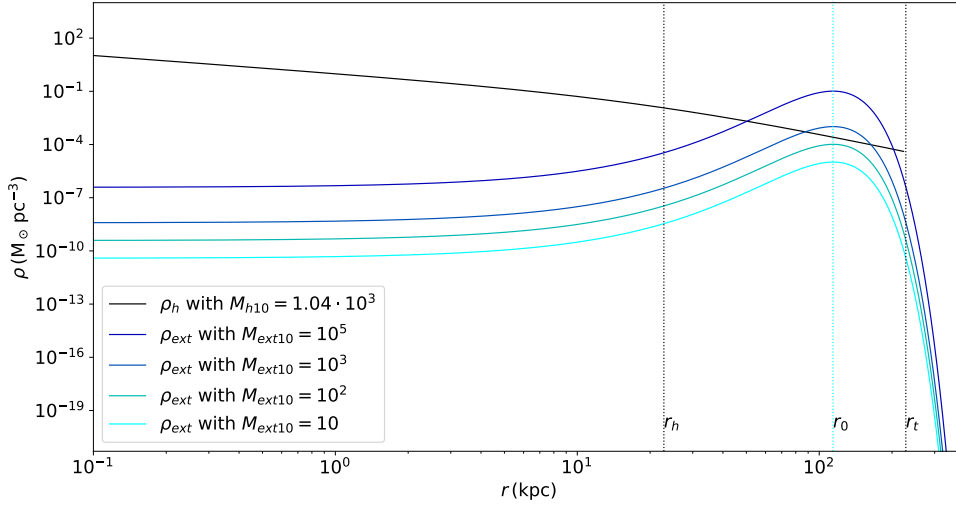

Figure 4.7: DM density profiles compared. Four *external* density profiles, with different mass, compared to the original NFW one. The NFW halo mass ($M_{h10} \equiv M_h/(10^{10}\,M_\odot)$) is calculated to reproduce σ_{e8}, while the external masses ($M_{ext10} \equiv M_{ext}/(10^{10}\,M_\odot)$) are arbitrarily fixed; r_h and r_t are, respectively, the scale and truncation radius of the NFW profile; r_0 is the centre of the external density profile, i.e. the peak of the external matter distribution. The main properties of these five models are given in table 4.3.
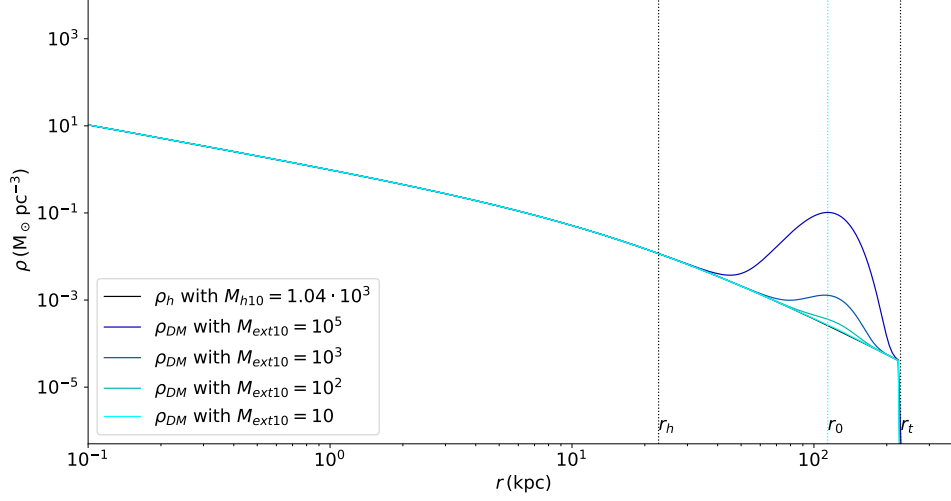
Figure 4.8: Total DM density profiles. Four *external* density profiles, with different mass, added to the original NFW one. The total density is the sum of the halo and external contributions: $\rho_{DM} = \rho_h + \rho_{ext}$. The first label refers to the model without external mass, i.e. DM density only due to the NFW one. The other models have the same NFW halo. For details about all features shown, see fig. 4.7 and table 4.3.

radius ($r \simeq r_0$). Since the halo is truncated and the external distribution is not, at radius larger than r_t, the latter dominates, but its density is essentially negligible with respect to values below r_t.

The code solves the JEs four times, now, computing the gravitational contribution to the stellar dynamics due to the central BH, stars, halo and finally to the external DM distribution. Thus, the expression 4.1 (section 4.1.1) becomes:

$$\sigma_{e8}^2 = \sigma_{**}^2 + \sigma_{*BH}^2 + \sigma_{*h}^2 + \sigma_{*ext}^2; \tag{4.20}$$

here the contribution to the squared projected central velocity dispersion, due to the total DM component, is $\sigma_{*DM}^2 = \sigma_{*h}^2 + \sigma_{*ext}^2$, where σ_{*h} and σ_{*ext} are obviously the velocity dispersion contributions due to the NFW halo and the external distribution, respectively. As previously seen, σ_{e8} can also be written by making explicit the mass of each component (stars and black hole together), so:

$$\begin{aligned}
\sigma_{e8}^2 &= M_{*10}\, \tilde{\sigma}_*^2 + \frac{M_{h10}}{f(c)}\, \tilde{\sigma}_{*h}^2 + M_{ext10}\, \tilde{\sigma}_{*h}^2 = \\
&= M_{*10}\, \tilde{\sigma}_*^2 + \alpha\, \tilde{\sigma}_{*h}^2 + \alpha_{ext}\, \tilde{\sigma}_{*h}^2,
\end{aligned} \tag{4.21}$$

in analogy with eq. 4.5, thus $\alpha_{ext} \equiv M_{ext10}$.
One could think that such a matter distribution does not influence the velocity dispersion profile in a region inner enough with respect to r_0, because here its density is negligible
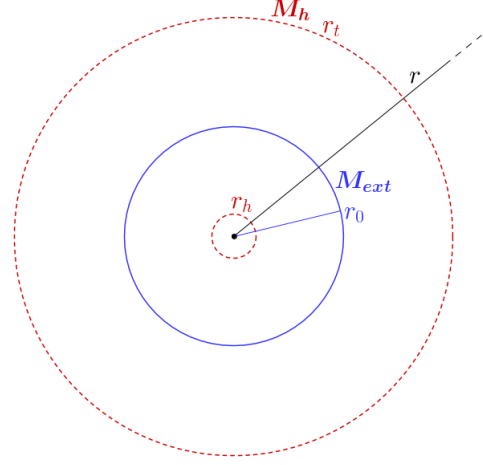
Figure 4.9: Shell scheme. Thought experiment of thin spherical shell representing the *external* DM distribution, in a system composed by a central BH, a smooth stellar distribution and a NFW DM halo. Proportions between r_0, r_h, r_t are kept.

and the distribution behaves as an external spherical shell, so the gravitational potential inside the shell is null, as stated from the *II shell theorem* of Isaac Newton. We are going to demonstrate, with a clear *thought experiment*, that this is not true, in principle. Although, in this way, we also show that the central velocity dispersion, in practice, is affected by this external distribution only if the latter is extremely massive.

We are going to consider, for simplicity, a spherical shell infinitely thin, containing a mass M_{ext} and located at r_0. The system composed by central BH, smooth stellar distribution, halo and shell is schematically illustrated in fig. 4.9. Since, in this thesis work, we are studying galaxies with spherical symmetry and an isotropic velocity dispersion tensor, we adopt the spherical coordinates. So the JE is simply

$$\frac{d(\rho_* \sigma^2)}{dr} = -\rho_* \frac{d\Phi}{dr}, \tag{4.22}$$

thus

$$\rho_* \sigma^2 = \int_r^\infty \rho_* \frac{d\Phi}{dr'} dr'. \tag{4.23}$$

The contribution due to the external shell is

$$\rho_* \sigma_{*ext}^2 = \int_r^\infty \rho_* \frac{d\phi_{ext}}{dr'} dr', \tag{4.24}$$

where the integral can be split in two parts, below and above r_0:

$$\begin{aligned} \rho_* \sigma_{*ext}^2 &= \int_r^{r_0} \rho_* \frac{d\phi_{ext}}{dr'} dr' + \int_{r_0}^\infty \rho_* \frac{d\phi_{ext}}{dr'} dr' = \\ &= -G \int_r^{r_0} \rho_* \frac{M_{ext}}{r'^2} dr' - G \int_{r_0}^\infty \rho_* \frac{M_{ext}}{r'^2} dr'. \end{aligned} \tag{4.25}$$

For the *II shell theorem*, the gravitational potential produced by the shell in the region below r_0 is null, so the first term is zero. Nevertheless, the second term is not zero and

it plays a role on the velocity dispersion profile; for the *I shell theorem*, the potential due to the shell above r_0 is that of a point mass M_{ext} concentrated in the galactic centre. Then eq. 4.25 becomes

$$\rho_*(r)\sigma^2_{*ext}(r) = -GM_{ext}\int_{r_0}^{\infty}\frac{\rho_*(r')}{r'^2}dr'. \tag{4.26}$$

This integral from r_0 to ∞ is obviously constant for $r < r_0$; moreover, ρ_* (modelled with a deprojected de Vaucouleurs profile, see fig. 3.1) is very low at radius $r > r_0$, so we can approximately consider that $\rho_*(r \geq r_0) \simeq \rho_*(r_0)$. The integral becomes

$$\int_{r_0}^{\infty}\frac{\rho_*(r)}{r^2}dr \simeq \frac{\rho_*(r_0)}{r}, \tag{4.27}$$

thus:

$$\sigma^2_{*ext}(r) \simeq \frac{GM_{ext}}{r}\frac{\rho_*(r_0)}{\rho_*(r)}. \tag{4.28}$$

We analyse now two limit situations:

$$\begin{cases} r \ll r_0 \Rightarrow \rho_*(r) \gg \rho_*(r_0) \Rightarrow \sigma^2_{*ext}(r) \simeq 0 \\ r \simeq r_0 \Rightarrow \rho_*(r) \simeq \rho_*(r_0) \Rightarrow \sigma^2_{*ext}(r) \simeq \dfrac{GM_{ext}}{r}. \end{cases} \tag{4.29}$$

We conclude that, in principle, the external DM distribution affects the central velocity dispersion of stars, but in practice its influence is negligible. This is true not only at $R_e/8$, but also at larger radii, e.g. $R_e/2$, R_e, $2\,R_e$. On the other side, its influence on the velocity dispersion profile is not negligible in a region near to the peak of the distribution.

In fig. 4.10, we show the velocity dispersion radial profile for the five study models, due to all the matter components (BH, stars, DM halo, external DM). It is well visible that the central velocity dispersion is not influenced by the addition of matter in the outer region of the galaxy, at least with a mass up to few orders of magnitude larger than the total mass of the galaxy. The contribution to the velocity dispersion, in fact, is not negligible at radius near to the peak of the external distribution, when its mass is at least comparable with the total mass; its impact becomes significant at inner radius, near to the halo scale radius, when the mass is at least two orders of magnitude larger than the total mass. Note that we are discussing here about the intrinsic velocity dispersion profile and not about the projected one, but obviously, since there are no variations in the intrinsic profile, there are no variations in the projected one too.

Therefore, these results suggest that producing observable variations of the velocity dispersion, i.e. variations in a region quite central to make observations possible, requires an amount of external mass many orders of magnitude larger than the total mass of the galaxy. It means that observations of the stellar velocity dispersion in the central region of galaxies (e.g. $R_e/8$, $R_e/2$, R_e, $2\,R_e$) are not able to reject the possibility of the presence of a dark matter distribution, even very massive, different from the well known NFW one, located in the outer region. We do not claim to propose the best description
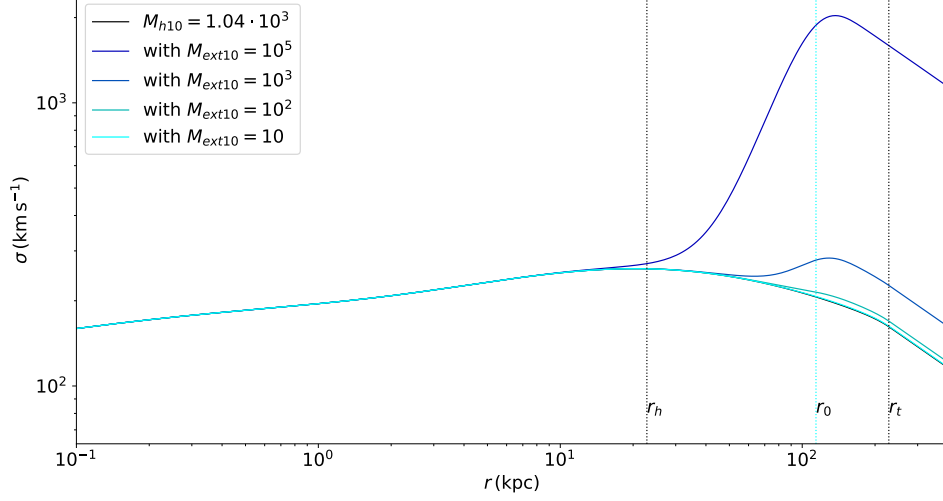
Figure 4.10: Velocity dispersion profile. Impact of the *external* DM distribution on the total velocity dispersion profile of stars, for four models with different external DM mass M_{ext}. The first label refers to the model without external mass; the other models have the same NFW halo. For details about all features shown, see fig. 4.7 and table 4.3.

for the DM density profile. We only note that a distribution rather different from the original NFW one is still consistent with observations of the kinematic field, taken in the central region; furthermore a large amount of DM could be contained in this component, without producing observables features in the central kinematic field.

Chapter 5

Discussions and conclusions

The aim of this thesis work was to investigate the amount and distribution of dark matter in early-type galaxies (ETGs), in relation with the properties of the stellar component and constrained by the projected velocity dispersion profile of stars. The motivation of this study, in addition to the obvious and practical interest in modelling ETGs, is due to the fact that cosmological predictions about the structure of DM halos (as obtained from N-body numerical simulations) are more focused on the general properties of halos than on a detailed description of well defined, specific objects. On average, cosmological simulations predict, in fact, a DM distribution following the celebrated NFW density profile, with a relation between the halo concentration and the total halo mass (given by $c \approx M_h^{-0.1}$).

With this thesis work, we attempted to look at the problem of a robust determination of the DM amount and distribution in galaxies, exploring the issue from two complementary points of view. A *top-down* approach, with priority given to cosmology, and a *bottom-up* approach, with priority given to the galactic astrophysics. The first one is based on theories of formation and evolution of structures in the Universe, while the second one is based on observations and dynamical modelling of galaxies and stellar populations. In practice, the adopted framework does not aim at confirm or disprove the predictions of cosmological simulations, but, on the contrary, to understand how much "freedom " observations allow about the structure of DM halos. In other words, we investigated how much the DM halo can vary while reproducing some observable kinematic properties, i.e. without producing unobserved features in the kinematic fields. In addition, we asked how much these results are affected by different factors, such as (1) structural properties of the stellar model: profile (e.g. de Vaucouleurs, Jaffe, Hernquist), shape (e.g. spherical symmetry, axisymmetry), degree of flattening, inclination angle with respect to the line of sight direction; (2) dynamical properties, like the anisotropy of the velocity dispersion tensor; (3) the aperture radius used to calculate the stellar velocity dispersion (e.g. $R_e/8$, $R_e/2$, R_e); (4) the stellar mass-to-light ratio; (5) the halo-to-stellar scale radius ratio.

We have already illustrated an overview of the issue of our interest, although, at the

present stage, we could not fully explore it in this thesis work, because of its complexity and the limited time available. However, we built accurate dynamical galaxy models as rigorous and at once flexible as possible, in order to be confident of our results and also to have the possibility to deepen our study in the future. This is accomplished by using the original numerical code JASMINE (first developed by Posacki et al., 2013), built to solve the Jeans equations, starting from a given stellar density profile and the gravitational potentials of the three components: stars, dark matter and central black hole. In our study, the stellar component is modelled by a spherical deprojected de Vaucouleurs density profile or an spherical Jaffe density profile, where the effective radius R_e and the luminosity in each band (e.g. L_V) are derived through the Scaling Laws (Faber-Jackson and Size-Luminosity), for a given value of the central velocity dispersion σ_{e8}. The DM component is modelled by a spherical NFW profile, whose β parameter (halo-to-stellar scale radius ratio) is fixed, while the concentration c is a free parameter. The stellar and dark masses are fixed to reproduce the central velocity dispersion characterising the model. Moreover, the mass of the supermassive black hole in the galactic centre is fixed to be three orders of magnitude less than the stellar mass. For a given σ_{e8}, and fixed the stellar component and the parameter β, we are able to obtain a *family* of halos characterised by the same ratio between the halo mass and a function of the concentration, but with different values of the halo mass and concentration.

The JASMINE code solves the Jeans equations in cylindrical coordinates for an axisymmetric and anisotropic system, described by a two-integral distribution function: thus, it calculates the velocity dispersion and the streaming velocity (non-zero only around the z-axis). These quantities are then projected along two lines of sight: face-on and edge-on. The code has been widely tested for several galaxy models, by modifying both structural properties (like the stellar distribution, the galaxy size, the halo parameters β and c) and technical properties, like the resolution of the grid. In this work, we have limited the variety of models to spherical and isotropic ones, with fixed β, and the aperture radius to $R_e/8$ only. Now we are going to summarise the main results achieved with this thesis work.

From a technical point of view, thanks to the linearity of the JEs, we derived a relation which allows us to vary both the total stellar mass and the total dark mass, reproducing a given σ_{e8}. We wrote this relation as a function of the stellar mass-to-light ratio ($\Upsilon_{* dyn}$), in order to compare $\Upsilon_{* dyn}$ inferred from our dynamical models with the known values obtained by Simple Stellar Population (SSP) synthesis models ($\Upsilon_{* pop}$). We chose a Kroupa IMF, because it is believed to describe the population formation in ETGs better than an IMF with a steeper slope at low masses (like the original Salpeter IMF). For a given σ_{e8}, we were able to find a *range* of halo masses consistent with $\Upsilon_{* pop}$ values, by considering the uncertainties on the estimated age and metallicity of the stellar population, derived from observations within a radius of $R_e/8$. In practice, we find a range for the dynamical $\Upsilon_{* dyn}$: from a *minimum* value (minimum age and metallicity), corresponding to the model with *minimum* stellar component and *maximum* DM halo, up to a *maximum* value (maximum age and metallicity), corresponding instead to the opposite limit case with *maximum* stellar component and *minimum* DM halo. We note

that, in any model family we studied (characterised by $\sigma_{e8} = 180, 210, 250\,\mathrm{km\,s^{-1}}$), stars and BH can reproduce the observed central velocity dispersion, without the addition of a DM component, with a value of Υ_{*dyn} within the acceptable range for Υ_{*pop}. In this case, this value of Υ_{*dyn} becomes the maximum stellar mass-to-light ratio possible for models defined by that σ_{e8}, because a larger value would not reproduce their central velocity dispersion. This also means that it is possible to build galaxy models, which are consistent with population synthesis results and uncertainties on measures within $R_e/8$ and do not require any DM fraction, at least for σ_{e8} between $180\,\mathrm{km\,s^{-1}}$ and $250\,\mathrm{km\,s^{-1}}$. The opposite limit model requires instead the maximum DM contribution, as written before, and provides M_h about two orders of magnitude larger than M_*. In conclusion, observations at $R_e/8$ allow stellar mass variations of about a factor of 2 and halo mass variations from 0 up to about $10^{13} - 10^{14}\,M_\odot$. In this way, we identify a region on the $c - M_h$ plane, populated by all halos reproducing the observations in the central region; while halos with mass and concentration values out of this region would require too low Υ_{*dyn}, i.e. too low M_*.

For illustrative purposes, we also considered a DM distribution different from the widely accepted NFW profile, to show there could exist alternative distributions which would be still consistent with observations of the central region of galaxies. As well known, the DM dominates with respect to the stellar component in the outer region of galaxies, where the stellar density tends to zero, while in the inner region the dominant component is the stellar one. Thus, the DM located at large radius has only a weak effect on the dynamics of stars at small radius. It is not surprising that the DM at radius large *enough* could not effect at all the central stellar dynamics. We questioned how much DM could be distributed in a region far *enough* from $R_e/8$, without conditioning the central velocity dispersion. For this purpose, we added to the NFW profile a DM component with a density profile as a gaussian distribution (isotropic), centred in the region where the NFW profile decreases as r^{-3}. We do not claim that this is the real DM distribution in ETGs, neither in spheroids in particular: it is a simple model showing some interesting points. First of all, σ_{e8} is not affected by this additional *external* dark mass, at least if this latter is up to some orders of magnitude larger than the NFW halo mass. That means it could exist a DM distribution, even very massive, in a region outer enough, unless the central stellar velocity dispersion would detect it. Furthermore, we note that a total DM profile different from the NFW one could not vary the trend of the velocity dispersion profile in the central region. Therefore, observations of σ_{e8} are not able to rule out the possibility of an alternative distribution, with respect to the generally accepted NFW one, and so, at the same time, they cannot be used to confirm that the DM halos are indeed well described by the NFW profile.

All the presented results suggest that the central stellar velocity dispersion is not a good diagnostic of the dark matter: it allows indeed a wide degeneracy between the parameters M_h and c and it does not constrain the amount and distribution of dark matter at large radius. In the next section, we are going to illustrate, in few points, the future plan for deepening and extending this preliminary study.

5.1   Future prospects

Our plan for future investigations is the exploration of different properties of ETGs, with the task of understanding how much the amount and distribution of dark matter are actually constrained by observations.

- First of all, we expect that observations within larger aperture radii (e.g. $R_e/2$, R_e) would provide more strict constraints on the dark matter, limiting the region in the $c - M_h$ plane populated by halos permitted by observations of the projected velocity dispersion.

- We will extend the present study to flat galaxies and investigate the effect of the degree of flattening.

- We will introduce the anisotropy of the velocity dispersion tensor and explore the effect of different degrees of anisotropy: first producing axisymmetric tensors and then studying triaxial tensors too.

- We will vary the halo-to-stellar scale radius ratio β, which determines the DM density profile: we expect that, as β increases, i.e. as the halo scale radius moves towards outer regions, the DM affects more and more the stellar dynamics; this would allow to constrain the dark matter content of galaxies in a more strict way.

- We will ask how much the influence of the DM on the stellar dynamics depends on their density profile (e.g. de Vaucouleurs, Jaffe, Hernquist) and on the inclination angle (FO, EO or other inclinations).

We conclude by remarking that, in our opinion, this work opens the door to a complementary study of ETGs, useful to better understand their dark and luminous contents.

Appendix A

Jeans equations

In this chapter we briefly show some considerations about stellar dynamics, especially in axisymmetric ETGs, to finally obtain the JEs in this particular case. For a deeper discussion, the reader is addressed, e.g., to Binney and Tremaine (2008), Ciotti (2000). Orbits of stars in galaxies, and stellar systems in general, are determined by the gravitational interactions with the stars themselves, the DM particles and the central BH, if present; while the gravitational effect of the gaseous component on stellar orbits can be neglected. For an exact investigation of the stellar dynamics, these systems should be treated as *N-body problems*, in which each encounter with a nearby star, DM particle or black hole, changes the position and the velocity of each star, i.e. its position in the phase-space $\gamma = (\boldsymbol{x}, \boldsymbol{v})$. Nevertheless, the time scale employed by a system to experience significant variations in its dynamics, through the sum of individual encounters, can be longer than its life time. This time is the so-called *2-body relaxation time* (t_{2b}) and it depends on the *crossing time* (t_{cross}) and total number of particles N of the system:

$$t_{2b} \sim \frac{N \, t_{cross}}{8 \ln N},\tag{A.1}$$

where $t_{cross} \simeq R/\sigma$ represents the characteristic time needed to cross a system of size R, moving at a speed σ. If t_{2b} is remarkably longer than its life time, 2-body collisions can be neglected and the system considered *collisionless*; otherwise the system has to be considered *collisional*. Note that the 2-body relaxation time increases with increasing t_{cross} and also with increasing N. The characteristic t_{2b} of a typical galaxy, with $N \simeq 10^{11}$ and $t_{cross} \simeq 10^8$ yr, is of the order of 10^7 Gyr, even greater than the age of the Universe; therefore, it is possible to obtain useful results about galactic dynamics even in the approximation of non-collisionality. After this assumption, we can indeed replace the discrete distribution of N stars with a continuous distribution $\rho(\boldsymbol{x}; t)$; the gravitational potential associated to this distribution derives from the Poisson equation $\nabla^2 \phi = 4\pi G\rho$:

$$\phi(\boldsymbol{x}, t) = -G \int_{\Re^3} \frac{\rho(\boldsymbol{\xi}; t) d^3\boldsymbol{\xi}}{||\boldsymbol{x} - \boldsymbol{\xi}||}.\tag{A.2}$$

The distribution of stars in the phase-space, at any time, is described by the so-called *distribution function* (DF) $f(\boldsymbol{x}, \boldsymbol{v}; t)$: a nowhere negative function, which represents the stellar mass density in a volume element of the phase-space $d^3\boldsymbol{x}d^3\boldsymbol{v}$, at a given time t. Just to clarify between different definitions in literature, we are adopting the definition of Ciotti (2000), while in Binney & Tremaine (1987) it is defined as a numerical density and in Binney & Tremaine (2008) as a probability density. So the stellar mass density distribution of the system, at any time, is given by

$$\rho(\boldsymbol{x}; t) = \int_{\Re^3} f(\boldsymbol{x}, \boldsymbol{v}; t)d^3\boldsymbol{v} \tag{A.3}$$

and the total stellar mass is

$$M = \int_\gamma f(\boldsymbol{x}, \boldsymbol{v}; t)d^3\boldsymbol{x}d^3\boldsymbol{v}. \tag{A.4}$$

Although stellar systems are never exactly collisionless, we have seen that galaxies essentially are, so we describe the time evolution of the DF in the assumption of *perfectly collisional regime*. Therefore the DF satisfy the so-called *collisionless Boltzmann equation* (CBE):

$$\frac{Df}{Dt} = \frac{\partial f}{\partial t} + \sum_{i=1}^{6} \frac{\partial(f\dot{w}_i)}{\partial w_i} = 0, \tag{A.5}$$

where w_i is the i-th coordinate of the phase space, i.e. $\boldsymbol{w} = (x_1, x_2, x_3, v_1, v_2, v_3)$, and $\dot{w}_i \equiv \frac{\partial w_i}{\partial t}$, so

$$\begin{cases} \dot{x}_i = v_i \\ \dot{v}_i = -\dfrac{\partial \Phi}{\partial x_i}. \end{cases} \tag{A.6}$$

The motion of each star is determined by the total gravitational potential Φ; in galaxies, considering the sum of the gravitational effects of stars themselves, DM and BH, it results $\Phi = \phi_* + \phi_{BH} + \phi_h$. The CBE can also be written as:

$$\frac{\partial f}{\partial t} + v_i \frac{\partial f}{\partial x_i} - \frac{\partial \Phi}{\partial x_i}\frac{\partial f}{\partial v_i} = 0, \tag{A.7}$$

where the Einstein summation convention (sum over repeated indices) is used.
Simpler differential equations are obtained through the *method of moments*: first of all, some functions are defined as velocity moments of the DF over the velocity space; then these quantities are used to find new equations (the *Jeans equations*) through the velocity moments of the CBE over the velocity space. We have already introduced the zero-order velocity moment at eq. (A.3): the stellar mass density $\rho(\boldsymbol{x}; t)$. The first-order moment is

$$\overline{v_i}(\boldsymbol{x}; t) := \frac{1}{\rho} \int_{\Re^3} v_i f d^3\boldsymbol{v} \tag{A.8}$$

and the second-order moments are

$$\overline{v_i v_j}(\boldsymbol{x}; t) := \frac{1}{\rho} \int_{\Re^3} v_i v_j f d^3\boldsymbol{v}, \tag{A.9}$$

$$\sigma_{ij}^2(\boldsymbol{x};t) := \frac{1}{\rho} \int_{\Re^3} (v_i - \overline{v_i})(v_j - \overline{v_j}) f d^3\boldsymbol{v} =$$
$$= \overline{(v_i - \overline{v_i})(v_j - \overline{v_j})} =$$
$$= \overline{v_i v_j} - \overline{v_i}\,\overline{v_j}, \tag{A.10}$$

for all $i,j = 1,2,3$. $\overline{v_i}$ is the i-th component of the streaming velocity, while σ_{ij}^2 is the velocity dispersion tensor, which represents the mean dispersion from the mean (stream-ing) velocity of stars. It is a symmetric tensor, so in a reference system in which it can be written in the diagonal form (e.g. the cylindrical coordinates system, as we will see later), the only non-zero components are $\sigma_{ii}^2 = \overline{v_i^2} - \overline{v_i}^2$. The geometrical interpretation as *velocity dispersion ellipsoid* is useful when the anisotropy of the velocity dispersion tensor plays an important role in determining the galaxy morphology, as generally happens in ETGs: in each point of the galaxy, and at any time, it is possible to define an ellip-soid, whose three semi-axis coincide with the three components of the diagonal tensor. If $\sigma_{ij}(\boldsymbol{x};t)^2 = \sigma^2(\boldsymbol{x};t)\delta_{ij} \, \forall \boldsymbol{x}$, the velocity dispersion tensor is called *isotropic* and the velocity dispersion ellipsoid is everywhere a sphere; otherwise σ_{ij}^2 is called *anisotropic*. For an investigation of the roles played in flattening the galaxy by the streaming velocity and the anisotropy of the velocity dispersion tensor, [–see intro–].

From the zero-order and first-order moments of the CBE (eq. (A.7)),

$$\int_{\Re^3} \left[\frac{\partial f}{\partial t} + v_i \frac{\partial f}{\partial x_i} - \frac{\partial \Phi}{\partial x_i} \frac{\partial f}{\partial v_i} \right] d^3\boldsymbol{v} = 0 \tag{A.11}$$

and

$$\int_{\Re^3} v_j \left[\frac{\partial f}{\partial t} + v_i \frac{\partial f}{\partial x_i} - \frac{\partial \Phi}{\partial x_i} \frac{\partial f}{\partial v_i} \right] d^3\boldsymbol{v} = 0, \tag{A.12}$$

the first and second Jeans equations (JEs) are respectively derived:

$$\frac{\partial \rho}{\partial t} + \frac{\partial(\rho\overline{v_i})}{\partial x_i} = 0, \tag{A.13}$$

$$\frac{\partial(\rho\overline{v_j})}{\partial t} + \frac{\partial(\rho\overline{v_i v_j})}{\partial x_i} + \rho\frac{\partial \Phi}{\partial x_j} = 0. \tag{A.14}$$

The latter can also be written in the following form:

$$\rho\frac{\partial \overline{v_j}}{\partial t} + \frac{\partial(\rho\sigma_{ij}^2)}{\partial x_i} + \rho\overline{v_i}\frac{\partial \overline{v_j}}{\partial x_i} + \rho\frac{\partial \Phi}{\partial x_j} = 0. \tag{A.15}$$

The reader can easily note the similarity between the two JEs for the stellar dynamics and the hydrodynamical equations of the mass conservation and the momentum conservation, respectively.

We consider now axisymmetric galaxies, in cylindrical coordinates (R, φ, z), and find the associated JEs. First of all, the velocity dispersion tensor is diagonal and aligned with the coordinate system. Then in a stationary and axisymmetric potential $\Phi(\boldsymbol{x})$, all derivatives with respect to t and φ vanish; the only non-zero streaming motion is in the azimuthal

direction ($\overline{v_R} = \overline{v_z} = 0$), there is no rotation in the radial and vertical directions, and so the only non-zero component of the angular momentum is $L_z = Rv_\varphi$; axisymmetry also impose $\overline{v_R^2} = \overline{v_z^2} = \sigma_R^2 = \sigma_z^2 \equiv \sigma^2$. A stationary and axisymmetric system is therefore described by a *two-integral* DF $f(H, L_z)$, which depends on the phase-space coordinates only through two integrals of motion (satisfying the *Jeans theorem*): the Hamiltonian $H = \frac{1}{2}(v_R^2 + v_\varphi^2 + v_z^2) + \Phi$ and the vertical component of the angular momentum L_z. The JEs in this case become:

$$
\begin{cases}
\dfrac{\partial(\rho_* \sigma^2)}{\partial z} = -\rho_* \dfrac{\partial \Phi}{\partial z} \\
\dfrac{\partial(\rho_* \sigma^2)}{\partial R} = \rho_* \dfrac{\overline{v_\varphi^2} - \sigma^2}{R} - \rho_* \dfrac{\partial \Phi}{\partial R}.
\end{cases}
\tag{A.16}
$$

Known the stellar mass density $\rho_*(\boldsymbol{x})$ and the total gravitational potential $\Phi(\boldsymbol{x})$, we have now two equations with two unknowns: σ^2 and $\overline{v_\varphi^2}$. In the next chapter (appendix B) we show how the resolution of these equations has been implemented in our numerical code JASMINE.

Appendix B

JASMINE code

Just to introduce to JASMINE (Jeans AxiSymmetric Models of galaxies IN Equilibrium), it is a numerical code initially developed by Silvia Posacki (Posacki et al., 2013; Posacki, 2014), then maintained by Andrea Negri and which I partially modified for this thesis work. It produces models of axisymmetric galaxies, solving the Jeans equations (JEs) in cylindrical coordinates (R, φ, z) for a distribution function (DF) depending on two integrals of motion, described in the previous appendix A. It is developed in `Fortran 90` and it can run in serial or parallel, using three processors. It works with three semi-logarithmic grids: a principal grid on which all quantities are computed and two secondary grids, staggered in R and z respectively, that serve to compute the derivatives with the centred finite-differences method of approximation. The extension and the precision (number of grid points) of the grids are established in order to include all the DM halo ($R_{max} = z_{max} > r_t$) and to resolve the central region accurately enough. Integrals are calculated with the standard trapezoidal rule.

The code receives as input the central luminosity-weighted velocity dispersion σ_{e8}, used to calculate the effective radius R_e; the degree of flattening q of the spheroid; the stellar and DM density profiles; the halo-to-stellar scale radius ratio β; the halo truncation radius r_t. The M_*, M_{BH} and M_h are fixed too. The code calculates the gravitational potential and the radial and vertical forces (per unit mass) associated to each component on the whole grid: through numerical integrations for the stellar component and through the analytical formula of chapter 2 for the BH and DM components. Now the Jeans equations are solved:

$$\begin{cases} \dfrac{\partial(\rho_*\sigma^2)}{\partial z} = -\rho_*\dfrac{\partial\Phi}{\partial z} \\ \dfrac{\partial(\rho_*\sigma^2)}{\partial R} = \rho_*\dfrac{\overline{v_\varphi^2} - \sigma^2}{R} - \rho_*\dfrac{\partial\Phi}{\partial R}. \end{cases} \tag{B.1}$$

From the first JE, the stellar velocity dispersion σ^2 is computed:

$$\rho_*\sigma^2 = \int_z^\infty \rho_*\frac{\partial\Phi}{\partial z'}dz'. \tag{B.2}$$

The natural boundary condition would be $\rho_* \sigma^2 \to 0$ for $r \to \infty$, thus the code calculates the solution of the vertical equation by solving the integral from z_{max} to each z, imposing $\rho_* \sigma^2 = 0$ at $z = z_{max}$. Then the second JE provides the total azimuthal velocity $\overline{v_\varphi^2}$. To calculate the ordered component $\overline{v_\varphi}^2$, representing the streaming motion, i.e. the rotation around the z-axis, we adopt the k-decomposition introduced by Satoh (1980):

$$\overline{v_\varphi}^2 = k^2(\overline{v_\varphi^2} - \sigma^2); \tag{B.3}$$

finally we calculate the azimuthal velocity dispersion from its definition:

$$\sigma_\varphi^2 \equiv \overline{v_\varphi^2} - \overline{v_\varphi}^2 = \sigma^2 + (1 - k^2)(\overline{v_\varphi^2} - \sigma^2). \tag{B.4}$$

The parameter k represents the amount of rotational support and it can be $0 \leq k \leq 1$: if $k = 1$ the galaxy is an isotropic rotator, so $\sigma_\varphi = \sigma_R = \sigma_z$ and it is totally rotationally supported; if $k = 0$ there is no net rotation ($\overline{v_\varphi}^2 = \overline{v_R}^2 = \overline{v_z}^2 = 0$), so the galaxy is supported only by the anisotropy of the velocity dispersion tensor; certainly, if $0 < k < 1$, the support is due to the sum of the contributions of rotation and anisotropy. We assume a constant value for k, although more realistic and complicated models would require that it is a function of (R, z), as considered by Ciotti and Pellegrini (1996) and by Negri et al. (2013).
The JEs are solved splitting the total gravitational potential in the different contributions of the three components,

$$\Phi = \phi_* + \phi_{BH} + \phi_h; \tag{B.5}$$

so they are solved three times, providing not only the total velocities, but also each contribution, which allows us to study individually the effect and the importance of each component on the stellar dynamics. In this way, for example, we obtain not only σ^2, but also σ_{**}^2, σ_{*BH}^2 and σ_{*h}^2.
Except those structural and dynamical properties of observed galaxies deducible from known empirical or theoretical relations, to compare properties of modelled galaxies with those of observed galaxies, we need to project them. The projections along a general l.o.s. of the stellar density ρ_*, the streaming velocity $\boldsymbol{v}$ and the velocity dispersion tensor $\boldsymbol{\sigma}^2$ are

$$\Sigma_* = \int_{-\infty}^{+\infty} \rho_* dl, \tag{B.6}$$

$$\Sigma_* v_{los} = \int_{-\infty}^{+\infty} \rho_* \langle \boldsymbol{v}, \boldsymbol{n} \rangle \, dl, \tag{B.7}$$

$$\Sigma_* \sigma_P^2 = \int_{-\infty}^{+\infty} \rho_* \langle \boldsymbol{\sigma}^2 \boldsymbol{n}, \boldsymbol{n} \rangle \, dl, \tag{B.8}$$

respectively. Where the brackets $\langle \, , \, \rangle$ indicate the scalar product, $\boldsymbol{n}$ is the l.o.s. direction, l is the integration path along $\boldsymbol{n}$. In general, σ_P^2 is different from the l.o.s. velocity dispersion σ_{los}^2, which is instead defined as:

$$\Sigma_* \sigma_{los}^2 = \int_{-\infty}^{+\infty} \rho_* \overline{(\langle \boldsymbol{v}, \boldsymbol{n} \rangle - v_{los})^2} dl = \Sigma_*(v_P^2 - v_{los}^2) = \Sigma_*(\sigma_P^2 + V_P^2 - v_{los}^2), \tag{B.9}$$

where

$$v_P^2 = \sigma_P^2 + V_P^2 = \sigma_{los}^2 + v_{los}^2, \tag{B.10}$$

as described in Ciotti & Pellegrini (1996). However in the particular cases of FO and EO views, or in case of absent streaming motion, it results $\sigma_P^2 = \sigma_{los}^2$. The FO projections are:

$$\Sigma_* = 2 \int_0^\infty \rho_* dz, \tag{B.11}$$

$$\Sigma_* \sigma_P^2 = \Sigma_* \sigma_{los}^2 = 2 \int_0^\infty \rho_* \sigma^2 dz. \tag{B.12}$$

The EO projections are instead:

$$\Sigma_* = 2 \int_R^\infty \frac{\rho_* R' dR'}{\sqrt{R'^2 - R^2}}, \tag{B.13}$$

$$\Sigma_* \sigma_P^2 = \Sigma_* \sigma_{los}^2 = 2 \int_R^\infty \left[\left(R'^2 - R^2 \right) \sigma^2 + R^2 \sigma_\varphi^2 \right] \frac{\rho_* dR'}{R' \sqrt{R'^2 - R^2}}, \tag{B.14}$$

$$\Sigma_* v_{los} = 2R \int_R^\infty \frac{\rho_* \overline{v_\varphi} dR'}{\sqrt{R'^2 - R^2}}, \tag{B.15}$$

$$\Sigma_* V_P^2 = 2R^2 \int_R^\infty \frac{\rho_* \overline{v_\varphi}^2 dR'}{R' \sqrt{R'^2 - R^2}}. \tag{B.16}$$

After the density projections, the FO and EO projected stellar masses are computed, integrating the surface densities. The FO and EO projected effective radius R_e are calculated as the radius containing half of the total projected stellar masses; the code also calculates $R_e/8$, used as the central radius. Finally, the corresponding luminosity-averaged aperture velocity-dispersions are calculated, for both the l.o.s., as follows:

$$\sigma_e^2 \equiv \frac{\int_0^{R_e} \Sigma_* \sigma_{los}^2 R dR}{\int_0^{R_e} \Sigma_* R dR}, \tag{B.17}$$

$$\sigma_{e8}^2 \equiv \frac{\int_0^{R_e/8} \Sigma_* \sigma_{los}^2 R dR}{\int_0^{R_e/8} \Sigma_* R dR}. \tag{B.18}$$

Our request is that the latter reproduce the input σ_{e8}.

Bibliography

Binney, J. (1978), 'On the rotation of elliptical galaxies', *MNRAS* **183**, 501–514.

Binney, J. and Tremaine, S. (1987), *Galactic dynamics.*

Binney, J. and Tremaine, S. (2008), *Galactic Dynamics: Second Edition*, Princeton University Press.

Cappellari, M. (2008), 'Measuring the inclination and mass-to-light ratio of axisymmetric galaxies via anisotropic Jeans models of stellar kinematics', *MNRAS* **390**, 71–86.

Cappellari, M. (2016), 'Structure and Kinematics of Early-Type Galaxies from Integral Field Spectroscopy', *ARAA* **54**, 597–665.

Cappellari, M., McDermid, R. M., Alatalo, K., Blitz, L., Bois, M., Bournaud, F., Bureau, M., Crocker, A. F., Davies, R. L., Davis, T. A., de Zeeuw, P. T., Duc, P.-A., Emsellem, E., Khochfar, S., Krajnović, D., Kuntschner, H., Lablanche, P.-Y., Morganti, R., Naab, T., Oosterloo, T., Sarzi, M., Scott, N., Serra, P., Weijmans, A.-M. and Young, L. M. (2012), 'Systematic variation of the stellar initial mass function in early-type galaxies', *Nature* **484**, 485–488.

Cappellari, M., McDermid, R. M., Alatalo, K., Blitz, L., Bois, M., Bournaud, F., Bureau, M., Crocker, A. F., Davies, R. L., Davis, T. A., de Zeeuw, P. T., Duc, P.-A., Emsellem, E., Khochfar, S., Krajnović, D., Kuntschner, H., Morganti, R., Naab, T., Oosterloo, T., Sarzi, M., Scott, N., Serra, P., Weijmans, A.-M. and Young, L. M. (2013), 'The ATLAS^{3D} project - XX. Mass-size and mass-σ distributions of early-type galaxies: bulge fraction drives kinematics, mass-to-light ratio, molecular gas fraction and stellar initial mass function', *MNRAS* **432**, 1862–1893.

Cappellari, M., Scott, N., Alatalo, K., Blitz, L., Bois, M., Bournaud, F., Bureau, M., Crocker, A. F., Davies, R. L., Davis, T. A., de Zeeuw, P. T., Duc, P.-A., Emsellem, E., Khochfar, S., Krajnović, D., Kuntschner, H., McDermid, R. M., Morganti, R., Naab, T., Oosterloo, T., Sarzi, M., Serra, P., Weijmans, A.-M. and Young, L. M. (2013), 'The ATLAS^{3D} project - XV. Benchmark for early-type galaxies scaling relations from

260 dynamical models: mass-to-light ratio, dark matter, Fundamental Plane and Mass Plane', *MNRAS* **432**, 1709–1741.

Ciotti, L. (2000), *Lecture notes on stellar dynamics*.

Ciotti, L. and Pellegrini, S. (1996), 'The energetics of flat and rotating early-type galaxies and their X-ray luminosity', *MNRAS* **279**, 240.

Ciotti, L. and Ziaee Lorzad, A. (2018), 'Two-component Jaffe models with a central black hole - I. The spherical case', *MNRAS* **473**, 5476–5491.

Davies, R. L., Efstathiou, G., Fall, S. M., Illingworth, G. and Schechter, P. L. (1983), 'The kinematic properties of faint elliptical galaxies', *ApJ* **266**, 41–57.

de Vaucouleurs, G. (1948), 'Recherches sur les nébuleuses extragalactiques', *Journal des Observateurs* **31**, 113.

Desroches, L.-B., Quataert, E., Ma, C.-P. and West, A. A. (2007), 'Luminosity dependence in the Fundamental Plane projections of elliptical galaxies', *MNRAS* **377**, 402–414.

Djorgovski, S. and Davis, M. (1987), 'Fundamental properties of elliptical galaxies', *ApJ* **313**, 59–68.

Dressler, A., Lynden-Bell, D., Burstein, D., Davies, R. L., Faber, S. M., Terlevich, R. and Wegner, G. (1987), 'Spectroscopy and photometry of elliptical galaxies. I - A new distance estimator', *ApJ* **313**, 42–58.

Dutton, A. A. and Macciò, A. V. (2014), 'Cold dark matter haloes in the Planck era: evolution of structural parameters for Einasto and NFW profiles', *MNRAS* **441**, 3359–3374.

Emsellem, E., Cappellari, M., Krajnović, D., Alatalo, K., Blitz, L., Bois, M., Bournaud, F., Bureau, M., Davies, R. L., Davis, T. A., de Zeeuw, P. T., Khochfar, S., Kuntschner, H., Lablanche, P.-Y., McDermid, R. M., Morganti, R., Naab, T., Oosterloo, T., Sarzi, M., Scott, N., Serra, P., van de Ven, G., Weijmans, A.-M. and Young, L. M. (2011), 'The ATLAS^{3D} project - III. A census of the stellar angular momentum within the effective radius of early-type galaxies: unveiling the distribution of fast and slow rotators', *MNRAS* **414**, 888–912.

Faber, S. M. and Jackson, R. E. (1976), 'Velocity dispersions and mass-to-light ratios for elliptical galaxies', *ApJ* **204**, 668–683.

Hubble, E. P. (1936), *Realm of the Nebulae*.

Jaffe, W. (1983), 'A simple model for the distribution of light in spherical galaxies', *MNRAS* **202**, 995–999.

Jeans, J. H. (1922), 'The Motions of Stars in a Kapteyn Universe', *MNRAS* **82**, 122–132.

Jester, S., Schneider, D. P., Richards, G. T., Green, R. F., Schmidt, M., Hall, P. B., Strauss, M. A., Vanden Berk, D. E., Stoughton, C., Gunn, J. E., Brinkmann, J., Kent, S. M., Smith, J. A., Tucker, D. L. and Yanny, B. (2005), 'The Sloan Digital Sky Survey View of the Palomar-Green Bright Quasar Survey', *AJ* **130**, 873–895.

Kormendy, J. (1977), 'Brightness distributions in compact and normal galaxies. II - Structure parameters of the spheroidal component', *ApJ* **218**, 333–346.

Kroupa, P. (2001), 'On the variation of the initial mass function', *MNRAS* **322**, 231–246.

Magorrian, J., Tremaine, S., Richstone, D., Bender, R., Bower, G., Dressler, A., Faber, S. M., Gebhardt, K., Green, R., Grillmair, C., Kormendy, J. and Lauer, T. (1998), 'The Demography of Massive Dark Objects in Galaxy Centers', *AJ* **115**, 2285–2305.

Maraston, C. (2005), 'Evolutionary population synthesis: models, analysis of the ingredients and application to high-z galaxies', *MNRAS* **362**, 799–825.

McDermid, R. M., Alatalo, K., Blitz, L., Bournaud, F., Bureau, M., Cappellari, M., Crocker, A. F., Davies, R. L., Davis, T. A., de Zeeuw, P. T., Duc, P.-A., Emsellem, E., Khochfar, S., Krajnović, D., Kuntschner, H., Morganti, R., Naab, T., Oosterloo, T., Sarzi, M., Scott, N., Serra, P., Weijmans, A.-M. and Young, L. M. (2015), 'The ATLAS^{3D} Project - XXX. Star formation histories and stellar population scaling relations of early-type galaxies', *MNRAS* **448**, 3484–3513.

Mellier, Y. and Mathez, G. (1987), 'Deprojection of the de Vaucouleurs R exp 1/4 brightness profile', *AAp* **175**, 1–3.

Navarro, J. F., Frenk, C. S. and White, S. D. M. (1996), 'The Structure of Cold Dark Matter Halos', *ApJ* **462**, 563.

Negri, A., Pellegrini, S. and Ciotti, L. (2013), 'Disk dynamics and the X-ray emission of S0 and flat early-type galaxies', *MemSAI* **84**, 762.

Poci, A., Cappellari, M. and McDermid, R. M. (2017), 'Systematic trends in total-mass profiles from dynamical models of early-type galaxies', *MNRAS* **467**, 1397–1413.

Posacki, S. (2014), *The dynamics of early-type galaxies as a tool to understand their hot coronae and their IMF.*

Posacki, S., Cappellari, M., Treu, T., Pellegrini, S. and Ciotti, L. (2015), 'The stellar initial mass function of early-type galaxies from low to high stellar velocity dispersion: homogeneous analysis of ATLAS^{3D} and Sloan Lens ACS galaxies', *MNRAS* **446**, 493–509.

Posacki, S., Pellegrini, S. and Ciotti, L. (2013), 'The effects of galaxy shape and rotation on the X-ray haloes of early-type galaxies', *MNRAS* **433**, 2259–2274.

Renzini, A. and Ciotti, L. (1993), 'Transverse Dissections of the Fundamental Planes of Elliptical Galaxies and Clusters of Galaxies', *ApJ* **416**, L49.

Salpeter, E. E. (1955), 'The Luminosity Function and Stellar Evolution.', *ApJ* **121**, 161.

Satoh, C. (1980), 'Dynamical Models of Axisymmetric Galaxies and Their Applications to the Elliptical Galaxy NGC4697', *PASJ* **32**, 41.

Sérsic, J. L. (1963), 'Influence of the atmospheric and instrumental dispersion on the brightness distribution in a galaxy', *Boletin de la Asociacion Argentina de Astronomia La Plata Argentina* **6**, 41.

Ringraziamenti

Ringrazio innanzitutto Luca Ciotti, prima ancora che come relatore, come professore: dai suoi corsi, ho iniziato ad apprendere un metodo prima di tutto di pensiero, di approccio alla materia scentifica in genere, e ho maturato l'interesse per la dinamica stellare in particolare. Come relatore, per avermi seguita in tutto il lavoro e indirizzata con importanti consigli e insegnamenti. Ringrazio Silvia Pellegrini, senza la quale questa tesi non sarebbe stata possibile, per l'attenzione e la pazienza con cui mi ha affiancata durante il lavoro sia di ricerca sia di scrittura. Ringrazio Andrea Negri, per la disponibilità con cui mi ha aiutata a muovermi nel magico mondo della programmazione. Un ringraziamento speciale a Cristiano Fanelli, come collega e come amico, con il quale ho condiviso il percorso di studio e di ricerca. Ringrazio tutti i miei colleghi, di triennale e di magistrale, con i quali ho trascorso i momenti di gioia e di fatica di questi anni. Ringrazio tutti i professori e ricercatori del Dipartimento di Fisica e Astronomia, che ho incontrato dal primo anno di triennale all'ultimo di magistrale, per gli insegnamenti e per la disponibilità e la gentilezza che ho sempre riscontrato.

Ringrazio la mia famiglia, i miei genitori, le mie sorelle, mio fratello, i miei nonni, per l'amore e la pazienza con cui mi sono sempre stati accanto: qualcuno con più amore; qualcuno con più pazienza; qualcuno con più interesse, prezioso e stimolante, per i miei studi; qualcuno con più ironia, non meno preziosa e stimolante. Ringrazio tutti gli amici e le amiche che ci sono stati e state in tutti questi anni, da vicino e da lontano. Un ringraziamento speciale a mia sorella Irene e a Marilù, che più di chiunque altro mi hanno supportata e sopportata in questi anni.